GEORG-AUGUST-UNIVERSITÄT
GÖTTINGEN

Fakultät für
Physik

Bachelor's Thesis

Akzeptanzstudien der $X \to SH \to b\bar{b}WW$ Analyse im 1-Lepton Zerfallskanal und der "Split-Boosted" Topologie für Run 3 im ATLAS-Experiment

Acceptance Challenge of the $X \to SH \to b\bar{b}WW$ Run-3 Analysis in the 1-Lepton Decay Channel and Split-Boosted Topology at ATLAS

prepared by

Monja Begau

from Göttingen

at the II. Physikalischen Institut

Thesis number: II.Physik-UniGö-BSc-2024/01

Thesis period: 23rd October 2023 until 19th February 2024

First referee: Prof. Dr. Stan Lai

Second referee: Prof. Dr. Ariane Frey

Zusammenfassung

In dieser Arbeit werden die Frameworks easyjet und SHbbVV, die beide unter anderem zur Suche nach $X \to SH \to bbVV$ genutzt werden, auf ihre Vergleichbarkeit untersucht. Der betrachtete Zerfallskanal ist dabei $X \to SH \to bbVV$ im 1-lepton Endzustand. Zum Vergleich wurden aufeinander aufbauende Selektionskriterien genutzt und die nach jedem Kriterium übriggebliebene Anzahl an Events verglichen. Es wurde beobachtet, dass beide Frameworks ähnliche Zahlen liefern, sich jedoch vor allem in der Auswahl an Events mit genau einem Lepton im Endzustand unterscheiden. Deshalb wurden sich die Verteilung verschiedener kinematischer Variablen der Leptonen und Jets in den übriggebliebenen Events beider Frameworks angeschaut. Aus diesen lässt sich vermuten, dass diese Unterschiede aus einer nicht übereinstimmenden Objekt-Rekonstruierung, vor allem in Bezug auf die Energie Kalibrierung, stammen.

Stichwörter: Higgs Boson, Resonante Higgs Produktion, easyjet, SHbbVV

Abstract

In this thesis, the frameworks easyjet and SHbbVV, which are both used to search for $X \to SH \to bbVV$, are analysed for their consistency. The decay channel under consideration is $X \to SH \to bbVV$ in the 1-lepton final state and the split-boosted topology. For comparison, successive selection criteria were used, and the number of events remaining after each criterion was compared. It was observed that both frameworks provide similar numbers, but differ mainly in the selection of events with exactly one lepton in the final state. Therefore, the distribution of different kinematic variables of the leptons and jets in the remaining events of both frameworks were analysed. From these, there are indications that these differences result from a mismatch in object reconstruction, especially with regard to energy calibration.

Keywords: Higgs boson, resonant Higgs production, easyjet, SHbbVV

Contents

1. Introduction

The Standard Model (SM) of particle physics aims to describe the fundamental particles and their interactions [1–8]. Many predictions made by the SM have been verified by numerous experiments, including the existence of the Higgs boson. In 2012, almost 60 years after its prediction, the Higgs boson was observed in the ATLAS and CMS experiments at the LHC [9], [10]. More experiments followed to study the properties of the Higgs boson and to further validate the predictions of the SM.

Although the SM can explain many observations made in experiments, it is not a complete theory. For example, gravity is the only fundamental force that is not included in the SM [11]. It also does not contain a particle that accounts for dark matter, which existence many astrophysics observations proposed [12]. Thus, there is a demand for searching for physics beyond this SM (BSM). This is for example done in the search for Higgs boson pair production. The non-resonant production of a Higgs boson pair is predicted by the Standard Model, whereas theories beyond the SM also predict resonant Higgs boson pair production, in which a scalar particle X produces two Higgs bosons. A further possible extension of this is the introduction of another scalar particle S, which allows the decay $X \to SH$ [13].

This bachelor thesis considers the $X \to SH \to b\bar{b}WW$ decay channel in the 1-lepton final state. One W boson thus decays hadronically, the other leptonically. The topology of this decay is strongly dependent on the masses of the X and S particles. Here, only the split-boosted topology is considered.

This work aims to compare two frameworks used to analyse this decay channel so that both frameworks can be used equally for further analysis without loss of comparability. This comparison is done based on a systematic and hierarchical sequence of selection criteria that were applied to three different signal samples in both frameworks. These samples are generated with Monte Carlo Simulation for three different mass points of X and S. The samples are made for Run 3 using a center of mass energy of $\sqrt{s} = 13.6$ TeV.

This thesis starts with an overview of the theoretical background regarding the Standard Model and in particular the resonant SH production in BSM theories in Chapter 2. In Chapter 3, this is followed by a description of the ATLAS detector at LHC. Afterward,

Chapter 4 describes the considered decay channel, as well as the event generation by Monte Carlo simulation. The object reconstruction and event selection that was used in this analysis is presented in Chapter 5, including the selection criteria that were used for the comparison of both frameworks. After that, the results of this are discussed in Chapter 6. In Chapter 7, the thesis is concluded and an outlook into further research possibilities is given.

2. The Standard Model of Particle Physics

The Standard Model of particle physics (SM) is the current description of particles and three of the four fundamental forces acting between these particles. Each of these forces is described via a quantum field theory (QFT). In order to describe the dynamics of this QFT, a Lagrangian is used, which contains the properties and interactions of the fundamental particles in the SM [1–8, 14–18].
The latest addition to the SM was the Higgs mechanism, which provides for the masses of the particles [19–24].

generation	quarks				leptons			
	symbol	mass	charge	spin	symbol	mass	charge	spin
I	u	2.3 MeV	2/3	1/2	ν_e	<2 eV	0	1/2
	d	4.8 MeV	-1/3	1/2	e	511 keV	-1	1/2
II	c	1.28 GeV	2/3	1/2	ν_μ	<190 keV	0	1/2
	s	95 MeV	-1/3	1/2	μ	105.7 MeV	-1	1/2
III	t	173.2 GeV	2/3	1/2	ν_τ	<18.2 MeV	0	1/2
	b	4.7 GeV	-1/3	1/2	τ	1.777 GeV	-1	1/2

Table 2.1.: The fermions of the Standard Model, their masses, charge and spin. Each doublet of quarks and leptons belongs to one generation. This table uses data from Ref. [25].

As shown in Table 2.1 and Table 2.2, the general distinction of fundamental particles is between fermions with spin $S = \frac{1}{2}$, gauge bosons with $S = 1$ and scalar bosons with $S = 0$.
The SM includes five gauge bosons, that are mediators of the fundamental forces: the electromagnetic force, the strong force and the weak force. The massless photon (γ) is the mediator of the electromagnetic force. The gluon (g) is also massless and mediates the strong force. The $W^\pm, Z^0$ bosons are massive and mediate the weak force.

Fermions are further divided into leptons and quarks. The latter carry colour charge and thus engage in the strong interaction. The SM incorporates six flavours of quarks

	symbol	mass	charge	spin
vector boson	g	-	-	1
	γ	-	-	1
	$W^{\pm}$	80.4 GeV	± 1	1
	Z	91.2 GeV	-	1
scalar boson	H	125.1 GeV	-	0

Table 2.2.: The bosons of the Standard Model, their masses, charge and spin. This table uses data from Ref. [25].

and six flavours of leptons, which are arranged in three generations in such a way that two quarks and two leptons are part of each generation. The generations differ only in the masses of the associated particles. The left-chiral particles are placed in weak isospin doublets. The electric charge of the particles in these doublets differs by one unit. For quarks, the doublet contains the up-type quark with electric charge $Q = +\frac{2}{3}$ and the down-type quark with $Q = -\frac{1}{3}$. The negatively charged leptons ($Q = -1$) are placed inside a doublet with their corresponding neutrino (ν), which do not carry electric charge. The down-type quarks in the isospin doublets and the negatively charged leptons respectively, possess a third component of weak isospin $I_3 = -\frac{1}{2}$. The up-type quarks and neutrinos have $I_3 = \frac{1}{2}$.
For every fundamental fermion in the SM exists an antiparticle with opposite additive quantum numbers. The right-chiral antifermions are also placed in weak isospin doublets. The right-chiral fermions and left-chiral antifermions are placed in weak isospin singlets.

2.1. The Strong Interaction (QCD)

The underlying symmetry of the strong interaction is the invariance under SU(3) local gauge transformations. There are three different colour charges (red, green and blue) and the corresponding anti-colours associated with this symmetry. The force carriers are gluons, that carry both colour and anti-colour charge. There are eight possible colour states for the gluon, which correspond to the generators of the SU(3) group [26, 27]. The gluon only couples to particles that also carry a colour charge. The effective potential of the strong interaction can be described as

$$V(r) = -\frac{\kappa}{r} + \frac{r}{a^2}, \tag{2.1}$$

where r is the distance between the quark and anti-quark and the constant $\frac{1}{a^2}$ is related to the strength of the linear term [28]. The constant κ describes the coupling strength of QCD. The coupling strength of the strong interaction depends on the energy scale of the interaction. At low energy scales, the coupling constant is large (close to one) and perturbation theory cannot be used to calculate low-energy QCD processes. At high energies, the coupling constant becomes sufficiently small such that perturbation theory can be used. This decrease of the coupling constant is called asymptotic freedom [29]. The linearly dependent term in this potential results in an increasing energy if two quarks are separated. As a result, only colourless particles can exist and quarks only appear in colourless bound states (hadrons). Particles consisting of a quark-antiquark pair are called mesons, whereas (anti)-baryons are particles consisting of three (anti)-quarks. The phenomenon that quarks are only observed as bound states is called quark confinement [30]. This concept also explains a process which is called hadronisation. This occurs if quarks are produced with high velocity. While the quarks are separated, the energy stored in the field of the strong potential between these two quarks increases, which leads to the production of particle anti-particle pairs. This process results in the production of hadron showers in particle colliders.

2.2. The Electroweak Interaction

The underlying symmetry of the electromagnetic interaction is the U(1) local gauge symmetry. The coupling to the electric charge of the fermions occurs via a massless photon. Due to the coupling to the electric charge, all charged leptons and quarks interact via the electromagnetic interaction [31–38].

The symmetry group of the weak interaction is the $SU(2)_L$ local gauge group. The quantum number related to the weak interaction is the weak isospin. Since all left-chiral fermions and right-chiral anti-fermions have a non-vanishing weak isospin, the charged gauge bosons of the weak interaction only couple to these particles. Right-chiral particles (and left-chiral anti-particles) are not affected and therefore have vanishing weak isospin. This property of the charged current weak interaction is emphasised using the subscript L.

Both theories are unified with the $SU(2)_L \times U(1)_Y$ symmetry group [1–3]. The index Y is the electroweak hypercharge $Y = 2(Q - I_3)$. The Higgs mechanism, described in Section 2.3, accounts for the masses of the observed physical gauge bosons. These bosons are linear combinations of the three gauge bosons from the $SU(2)_L$ symmetry (W^1, W^2, W^3)

and the gauge boson B from the $U(1)_Y$ symmetry[1]

$$W_\mu^\pm = \frac{1}{\sqrt{2}}(W_\mu^1 \mp iW_\mu^2) \tag{2.2}$$

$$Z_\mu = -\sin(\theta_W)B_\mu + \cos(\theta_W)W_\mu^3 \tag{2.3}$$

$$A_\mu = \cos(\theta_W)B_\mu + \sin(\theta_W)W_\mu^3\,, \tag{2.4}$$

where A_μ is the photon field and θ_W the Weinberg mixing angle. As stated before, the $W^\pm$ bosons solely couple to left-chiral particles. This property is described in the vertex factor via the projection operator $1-\gamma^5$, that projects the state into its left-chiral component. The charged currents of the weak interaction are mediated via the $W^\pm$ boson and always change the flavour of the interacting particles. For leptons, this flavour change is only possible within a generation, whereas quarks can change their flavour from any up-type to any down-type quark, but not with the same transition probability. In the vertex factor for the charged weak interaction of quarks, the different transition probabilities are expressed via the CKM matrix element V_{ij} [39, 40]. The vertex factor for the weak interaction for leptons is [3–5]

$$i\frac{g_W}{2\sqrt{2}}\gamma^\mu(1-\gamma^5)\,, \tag{2.5}$$

and for quarks

$$i\frac{g_W}{2\sqrt{2}}\gamma^\mu(1-\gamma^5)V_{ij}\,, \tag{2.6}$$

where g_W is the coupling constant of the $SU(2)$ symmetry.
The Z^0 boson, as a superposition of the $U(1)_Y$ and $SU(2)_L$ fields, couples to both the electric charge and the weak isospin. Therefore, it couples to both left-handed and right-chiral particles, but not with the same strength. This property can be seen in the vertex factor for the neutral current mediated by the Z boson [2]

$$i\frac{g_z}{2}\gamma^\mu(2Q\sin^2(\theta_W) + I_3(1-\gamma^5)). \tag{2.7}$$

Furthermore, the Z^0 boson is not capable of mediating flavour changing currents.

2.3. The Higgs Mechanism

Particles in the SM gain their masses through interactions with the Higgs field [19–24]. To preserve invariance of the SM Lagrangian under the $SU(2)_L \times U(1)_Y$ local gauge transformation, the four gauge bosons need to be massless, although the observed gauge bosons of the weak interaction are not massless. The Higgs mechanism extends this theory,

so they acquire mass by interacting with a field with non-zero expectation value [19–21]. Two complex scalar fields, which are placed in a weak isospin doublet ϕ, are added to the SM Lagrangian [2, 3]. As before, the charge of the components of this doublet differs by one unit of the electric charge. The corresponding potential,

$$V = \mu^2(\phi^\dagger\phi) + \lambda(\phi^\dagger\phi)^2 \tag{2.8}$$

with the two constants λ and μ, is added to the Lagrangian [2].
In order to have a finite minimum, the theory requires $\lambda > 0$. The introduction of spontaneous symmetry breaking through $\mu^2 < 0$ gives an infinite set of minima in a distance v from the origin for this potential. This is called spontaneous symmetry breaking since the ground state of the system does not respect the symmetry of the system anymore. In addition, the ground state of the doublet is chosen as

$$< \phi >_v = \frac{1}{\sqrt{2}} \begin{pmatrix} 0 \\ v \end{pmatrix}, \tag{2.9}$$

where $v = -\mu^2/\lambda$ is the vacuum expectation value. The complex scalar fields are then rewritten as expansion around this vacuum state and written in unitary gauge [41]

$$\phi = \frac{1}{\sqrt{2}} \begin{pmatrix} 0 \\ v + h(x) \end{pmatrix}, \tag{2.10}$$

where $h(x)$ is the physical Higgs field. The Higgs boson is the excitation of this field.
By writing the Lagrangian such that it respects the $SU(2)_L \times U(1)_Y$ local gauge symmetry the mass terms of the gauge bosons can be obtained. The masses of the physical fields written in Equation 2.4 can be parameterised as

$$m_W = \frac{1}{2} g_W v \tag{2.11}$$

$$m_Z = \frac{1}{2} v \frac{g_W^2}{\cos(\theta_W)} \tag{2.12}$$

$$m_A = 0 \tag{2.13}$$

at leading order.
From the Higgs mechanism, one can also obtain the interaction terms between the $W^\pm$ and Z^0 bosons. After symmetry breaking, the Higgs potential can be written as:

$$V(h) = \frac{1}{2} m_H h^2 + \lambda v h^3 + \lambda h^4, \tag{2.14}$$

where $m_H = \sqrt{\lambda}v$ is identified as the Higgs boson mass. As can be seen in Equation 2.14, the Higgs mechanism predicts three- and four-point self-interactions of the Higgs boson. The Higgs mechanism can also be used to generate the masses of fermions. Again, the fermion masses cannot be placed directly into the Lagrangian, but are introduced via the term [2]

$$\mathcal{L}_m = -g_f \left[\bar{f}_L \phi f_R + \bar{f}_R \bar{\phi} f_L \right], \tag{2.15}$$

where g_f is the coupling strength of the fermion to the Higgs field. In unitary gauge for the Higgs doublet ϕ, this yields a mass term with a mass of

$$m_f = \sqrt{2}\frac{g_f}{v}, \tag{2.16}$$

and an interaction term proportional to the coupling strength g_f. This procedure yields only the masses for the lower components of the weak isospin doublets. For quarks the masses of the upper component are obtained similarly by using the conjugate doublet of ϕ

$$\phi_c = -\frac{1}{\sqrt{2}} \begin{pmatrix} v + h(x) \\ 0 \end{pmatrix}. \tag{2.17}$$

2.4. Higgs Boson Properties

The SM predicts the spin of the Higgs boson to be 0 and the parity to be positive. Both Atlas and Cms collaborations reported the observation of a new boson with a mass of $m_H = 125$ GeV and these properties in 2012 [9, 10].

2.4.1. Higgs Boson Production and Decay

In principle, the Higgs boson can decay to all massive particles in the SM except into $t\bar{t}$, which is kinematically not allowed. Since the coupling of the Higgs boson to other particles is proportional to their masses, the branching ratios (BR) of the decays are highest for more massive particles. As can be seen from the branching ratios of the Higgs boson in Table 2.3, the dominant decays are the decay into $b\bar{b}$ and into two W bosons. Despite the greater mass of the W boson, this decay is suppressed since $2m_W > m_H$ and therefore, at least one W boson in the decay needs to be off-shell. In Table 2.4, the cross-sections of different production modes, predicted by the SM, are shown for proton-proton collisions at Lhc $\sqrt{s} = 13.6$ TeV. The most dominant process is gluon-gluon fusion (ggF), where the production of the Higgs boson is mediated via a virtual quark loop, which is produced via two gluons. The virtual quark loop is dominated by top or bottom quarks since they

Decay channel	Branching ratio
$H \to b\bar{b}$	$5.82 \cdot 10^{-1}\ ^{+1.2\%}_{-1.3\%}$
$H \to W^+W^-$	$2.14 \cdot 10^{-1}\ ^{+1.5\%}_{-1.5\%}$
$H \to \tau^+\tau^-$	$6.27 \cdot 10^{-2}\ ^{+1.6\%}_{-1.6\%}$
$H \to c\bar{c}$	$2.89 \cdot 10^{-2}\ ^{+5.5\%}_{-2.0\%}$
$H \to ZZ$	$2.62 \cdot 10^{-2}\ ^{+1.5\%}_{-1.5\%}$
$H \to \gamma\gamma$	$2.27 \cdot 10^{-3}\ ^{+2.1\%}_{-2.1\%}$

Table 2.3.: Branching ratios for different decay channels of the Higgs boson [25]

have the highest masses. Vector boson fusion (VBF) describes the process of two W or two Z bosons coupling to the Higgs boson after being radiated off of two quarks. In the Higgs Strahlung (WH/ZH) process, a quark anti-quark pair couples to a W or Z boson, which then radiates of a Higgs boson. The mode with the smallest cross-section is the associated production of a top quark pair (ttH), in which two gluons each decay into a $t\bar{t}$ pair. Afterwards a $t\bar{t}$ pair couples to a Higgs boson. The Feynman diagrams of the two most dominant processes at the LHC are also shown in Figure 2.1

Production mode	cross-section [pb]
ggF	$52.2^{+5.6\%}_{-7.4\%}$
VBF	$4.1^{+2.1\%}_{-1.5\%}$
WH	$1.46^{+1.8\%}_{-1.9\%}$
ZH	$0.95^{+4.0\%}_{-3.6\%}$
$t\bar{t}H$	$0.61^{+6.9\%}_{-9.8\%}$
total	55.1

Table 2.4.: Cross-sections for different Higgs production modes in proton-proton collisions at $\sqrt{s} = 13.6$ TeV for $m_H = 125$ GeV [25]

2.4.2. Non-Resonant Higgs Boson Pair Production

As seen in Equation 2.14, the SM predicts three- and four-point self-interactions of the Higgs boson, whose strength is characterised by the self-coupling constant λ. The trilinear self-coupling of the Higgs boson occurs in pair production of the Higgs boson. The leading production mode of the Higgs pair production at the LHC is again the loop induced ggF, that is mediated mainly by top-quark loops [42]. The leading order of this production mode has two contributions, the box and triangle diagrams, which are shown in Figure 2.2 [43]. The triangle diagram includes the Higgs self-coupling.

Both processes interfere destructively, which results in a low cross-section of 31.05 ± 1.90 fb in proton-proton collisions at $\sqrt{s} = 13$ TeV, compared to the ggF cross-section of

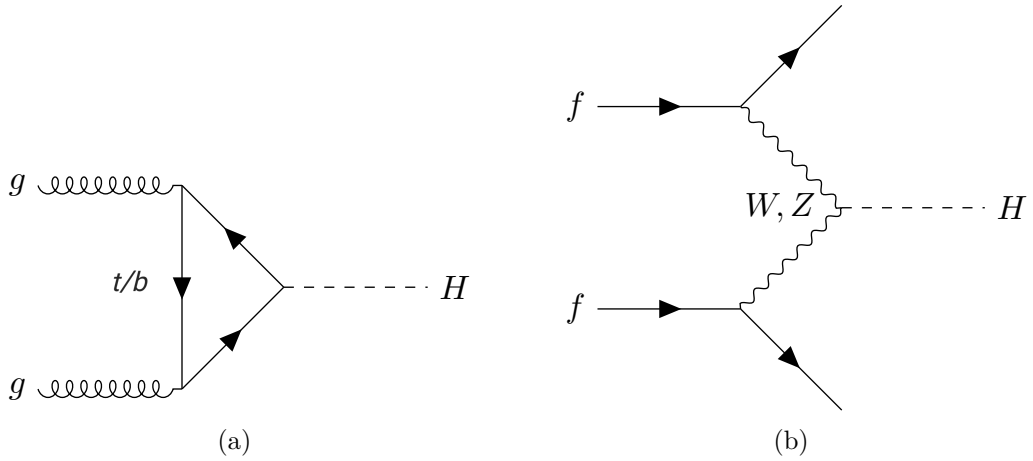

Figure 2.1.: Feynman diagrams of the leading order of the two most dominant production modes for the Higgs boson at the LHC: (a) ggF and (b) VBF.

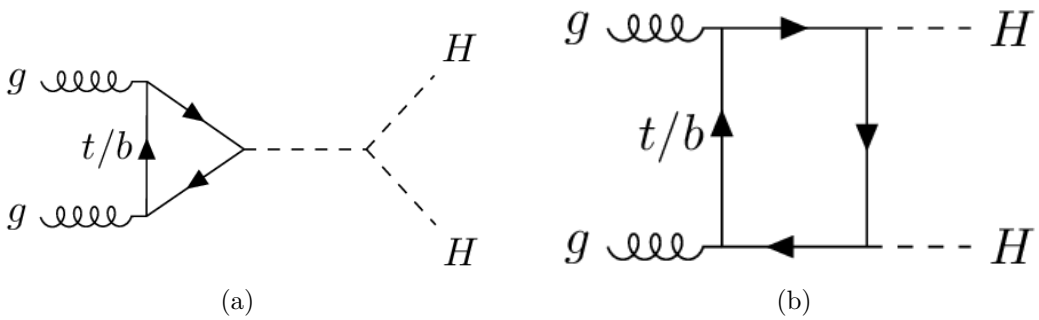

Figure 2.2.: The triangle diagram of the Higgs pair production, that includes (a) Higgs self-coupling and (b) the box diagram of the Higgs pair production [43]

single Higgs production in Table 2.4 [43].
The described pair production is referred to as non-resonant. Beyond the SM theories can predict resonant Higgs pair production, if there exist one or more particles that are capable of decaying resonantly into a Higgs boson pair [44–46].

2.5. Beyond the Standard Model

Although the Standard Model can explain many observations made in particle physics it is not a complete theory and has its limitations. Therefore, physicists search for theories beyond the SM in order to solve problems the Standard Model cannot explain. A few problems are presented in the following.
In the SM, all fundamental forces are included except gravity since the gravitational force is weak compared to the other forces and negligible up until the Planck energy scale of

$\mathcal{O}(10^{19})$ [11]. As seen before, the fundamental forces in the SM are described by quantum field theory, whereas gravity is described by general relativity. Bringing these two theories together presents great theoretical difficulties.
Another phenomenon that the Standard Model does not describe is dark matter. Many astrophysical observations indicate that, apart from the visible matter, the universe also consists of matter, that does not emit, absorb or reflect light, the so-called dark matter [12].
Further extensions of the Standard Model can be made in the Higgs sector. One possibility is to add one or more scalar particles so that the production of Higgs boson pairs can occur not only non-resonantly, but also resonantly. The simplest way of extending the Higgs Sector is adding a real scalar singlet, so a heavy scalar particle can decay into two Higgs bosons [47].
To obtain two different scalar particles as decay products one can add a second real scalar singlet. This extension is called the two real scalar singlet model (TRSM) [13]. Through this, two scalar particles X and S are added to the SM. In the mass eigenstates of these scalar particles X is assumed to be the heaviest scalar particle and the Higgs boson is assumed to be the lightest. This model allows self-couplings and couplings between X, S and H, so the decay $X \to SH$ is possible. To ensure that S and H are produced on shell,

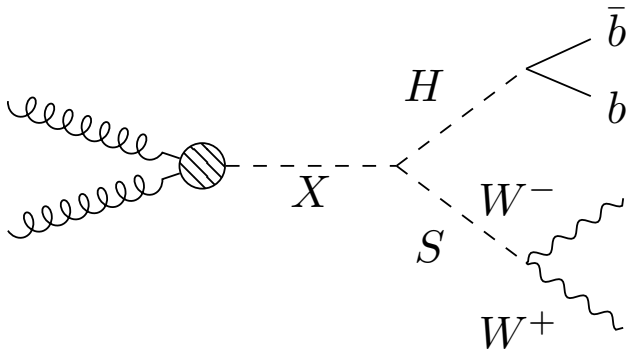

Figure 2.3.: Schematic diagram of the resonant production of the scalar singlet S and the H boson through the resonance X. The H boson further decays into a $b\bar{b}$ pair and the S decays into two W bosons.

one requires $m_X > m_S + m_H$. As mentioned before, the decay $H \to b\bar{b}$ has the highest BR. The coupling of S to SM particles follows the one of the Higgs boson. Therefore, if the mass of the scalar particle S is assumed to be $m_S > 2m_W$, the decay $S \to WW$ has the highest BR since both W bosons can be produced on shell. This decay is depicted in

Figure 2.3.
As this model does not predict the masses of the scalar particles, one must consider wide mass ranges for X and S. The mass distributions influence the kinematics of the final states and thus affect the topology of the decay. The decay topologies are further discussed in Chapter 4.

3. Experimental Setup

3.1. The LHC

The LHC is a synchrotron with a circumference of 27 km that is located in Geneva [48]. It is designed to accelerate protons and heavy ions.
Before particles are injected into the LHC, they pass through various preaccelerators [48]. The LHC accelerator chain is shown in Figure 3.1. It starts with the linear accelerator Linac4, that accelerates negative hydrogen ions. As these ions are injected into the Proton Synchrotron Booster (PSB), they are stripped of their electrons. The leftover protons are further accelerated in the PSB, the Proton Synchrotron (PS) and the Super Proton Synchrotron (SPS) up to a beam energy of 450 GeV. After that, the protons are injected into the two beams of the LHC, where one beam circulates clockwise and the other beam counterclockwise. The beams are further accelerated and are collided inside the four detectors ALICE, ATLAS, CMS and LHCb at a center of mass energy of $\sqrt{s} = 13.6$ TeV for Run 3.

3.2. The ATLAS Detector

A schematic view of the ATLAS detector is shown in Figure 3.2. It consists of the Inner Detector (ID) that tracks charged particles and measures their momentum, the calorimeter system that is mainly used for energy measurements, and a muon spectrometer that is used to track muons [50].

3.2.1. Coordinate System

The origin of the orthogonal right-handed coordinate system used for describing the particle collisions in the ATLAS detector is chosen as the interaction point. The beam direction marks the z-axis. The positive x-direction points to the center of the LHC ring and the y-axis points upwards such that the x-y plane is transverse to the beam axis. Furthermore, the azimuthal angle ϕ is measured around the beam axis and the polar angle is defined

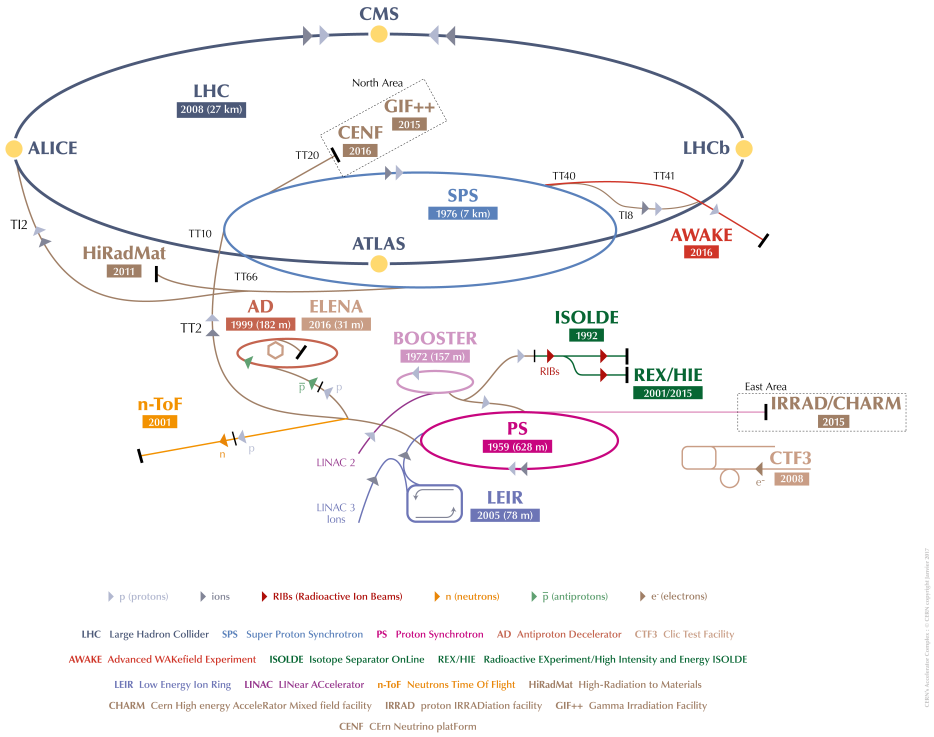

Figure 3.1.: Illustration of the CERN accelerator complex [49].

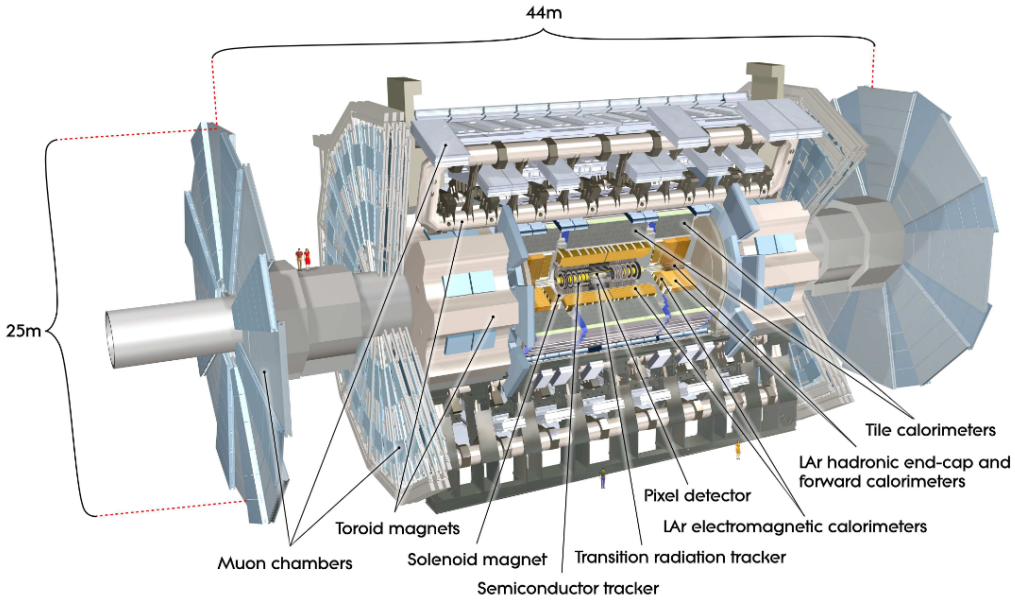

Figure 3.2.: Illustration of the ATLAS detector with its different layers [50].

relative to the z-axis.
In addition to that the rapidity y is defined as

$$y = \frac{1}{2} \ln \left(\frac{E + p_z}{E - p_z} \right). \tag{3.1}$$

This definition is useful since the difference in the rapiditiy (Δy) is invariant under Lorentz boosts in z-direction. y is used in case of massive objects, and in the ultra relativistic limit ($m \ll |\vec{p}|$) the pseudorapidity η can be used, that is defined as

$$\eta = -\ln(\tan(\theta/2)). \tag{3.2}$$

The transverse momentum p_T, transverse energy E_T and the missing transverse momentum E_T^{miss} are defined in the x-y plane. The distance ΔR in the η-ϕ space is $\Delta R = \sqrt{\Delta\eta^2 + \Delta\phi^2}$.

3.2.2. The Inner Detector

The Inner Detector (ID) is the innermost detector and provides tracking and vertex measurements as well as electron identification. It is contained in a cylinder around the colliding proton beams. The ID is situated in a solenoid magnetic field of 2 T, in which charged particles move on bend tracks due to the Lorentz force. This setup is important to measure the transverse momentum of the particles. The Inner Detector consists of three subsystems, the pixel and strip detectors and a transition radiation tracker (TRT). In total, the Inner Detector covers a pseudorapidity range of $|\eta| < 2.5$. The momentum resolution of the ID is $\sigma_{p_T}/p_T = 0.05\%\ p_T \oplus 1\%$. An illustration of the ID is shown in Figure 3.3

The pixel detector is a semiconductor tracker and is the detector system closest to the interaction point due to its good spatial resolution. It tracks the path of traversing charged particles. Compared to the other subsystems of the ID, the pixel detector provides the smallest number of measuring points since it covers the smallest area, but has the best resolution. The electrode of the semiconductor is segmented into pixels of $50 \times 400\ \mu\text{m}^2$ and each module of the pixel detector hosts 47232 pixels. The modules are placed on four cylindrical layers and three end-cap detectors on each side. The cylindrical layers are installed parallel and the end-cap detectors perpendicular to the beam. The innermost layer, the insertable B-layer (IBL) was later installed in 2014 in order to restore the b-tagging efficiency and improve the vertex and b-tagging performance. It is inserted at a radius of 3 cm and the pixel of the IBL have a size of $50 \times 250\ \mu\text{m}$.

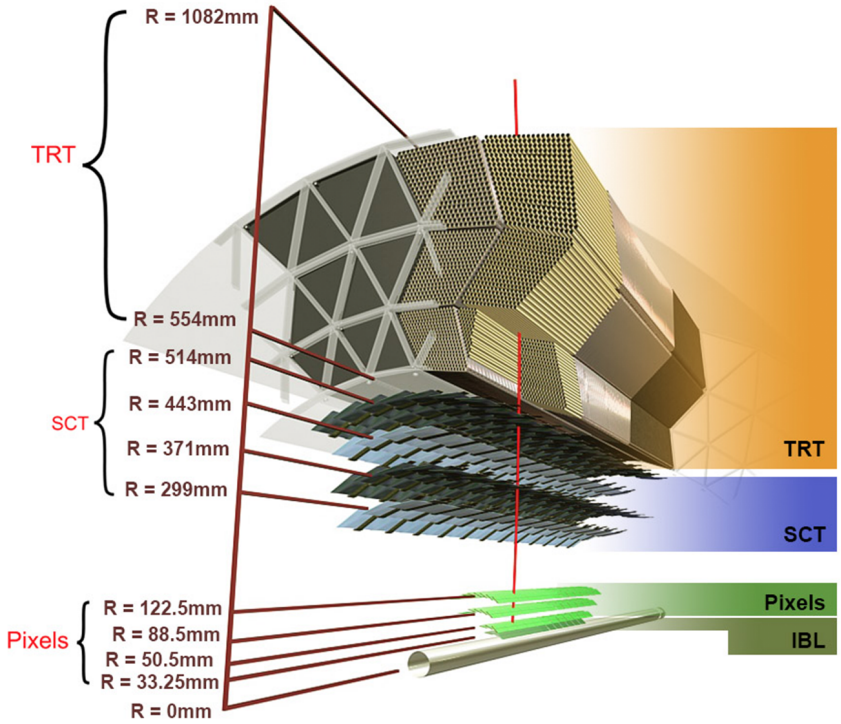

Figure 3.3.: Illustration of the ATLAS Inner Detector with the IBL as nearest part around the proton beam, followed by the pixel and semiconductor detectors. The largest subsystem of the ID is the TRT.

Strip Detector

Like the pixel detector, the second subsystem consists of a semiconductor tracker whose electrodes are divided into strips. This results in a lower spatial resolution but is connected with lower material costs, so a wider area can be covered compared to the pixel detector. The strips are placed on modules with a 80 μm pitch. The over 4000 modules are again placed on four cylindrical layers around the beam axis and on nine disks on each side, where the strips are arranged radially to the beam axis. The modules consist of four silicon detectors, two on either side. These sides are rotated by 40 mrad which provides a two-dimensional measurement of the tracking points and reduces ambiguities in the reconstruction of the measurement. The pixel detector and strip detector together cover a range of $|\eta| < 2.5$.

Transition Radiation Tracker

The TRT is the outermost subsystem of the Inner Detector, which has the lowest spatial resolution of all subsystems of the ID. It covers the largest area and gives therefore the

most measurement points for the track reconstruction. The modules are made of 329 to 729 parallel proportional drift tubes, which are filled with a gas mixture of Ar, CO_2 and O_2. Particles, that are passing the drift tubes, ionise the gas, which causes an electrical current in the nearest wire. Tracks are then reconstructed from drift time measurements. The momentum resolution of the TRT is $\sigma_{p_T}/p_T = 0.05\% \cdot p_T \oplus 1\%$ and it covers a pseudorapidity range of $|\eta| < 2.0$.
Besides the track reconstruction, the TRT is capable of identifying electrons due to an effect called transition radiation, which is caused by charged particles passing through inhomogeneous media. The emitted electromagnetic wave is absorbed in the gas and produces a much larger signal amplitude than the ionised gas. The probability of the transition radiation increases with $\gamma = E/m$, so the intensity of this radiation increases for lighter particles. Thus, this effect is used to distinguish between tracks originating from hadrons or electrons. Particle tracks with very strong signals can be identified as originating from an electron.

3.2.3. Calorimeter

The calorimeter provides position and energy measurements of electromagnetically and strongly interacting particles. These measurements are based on the concept of particle showers. Particles that pass through the calorimeter interact with its material, creating secondary particles that also interact with the material and produce particle showers. The shower stops, if the particles reach a critical energy and the particles are absorbed by the material. Since electrons only interact electromagnetically with the calorimeter material, whereas hadrons and gluons mainly interact strongly, the behaviour of both particle showers is different. Thus, the calorimeter is divided into the electromagnetic and hadronic calorimeter. An illustration of the calorimeter is shown in Figure 3.4.
Electromagnetic calorimeters are based on the production of secondary particles through Bremsstrahlung and pair production, whose energy can be measured. The ATLAS electromagnetic calorimeter is a sampling calorimeter, in which the active material is made up of liquid argon (LAr). The absorber (passive material) is made of lead, steel and copper. Passing particles ionise the LAr, producing a measurable current.
The electromagnetic LAr calorimeter is divided into a barrel part and two end-caps, which together cover a region of $|\eta| < 3.2$. The energy resolution of endcaps and barrel is $10\%/\sqrt{E} \oplus 0.7\%$ for electromagnetic showers. The thickness of the electromagnetic calorimeter (with endcaps) is more than 24 radiation lengths (X_0) and 11 interaction lengths (λ). The electromagnetic calorimeter also contains a presampler detector that corrects for energy losses if a particle starts showering before reaching the calorimeter

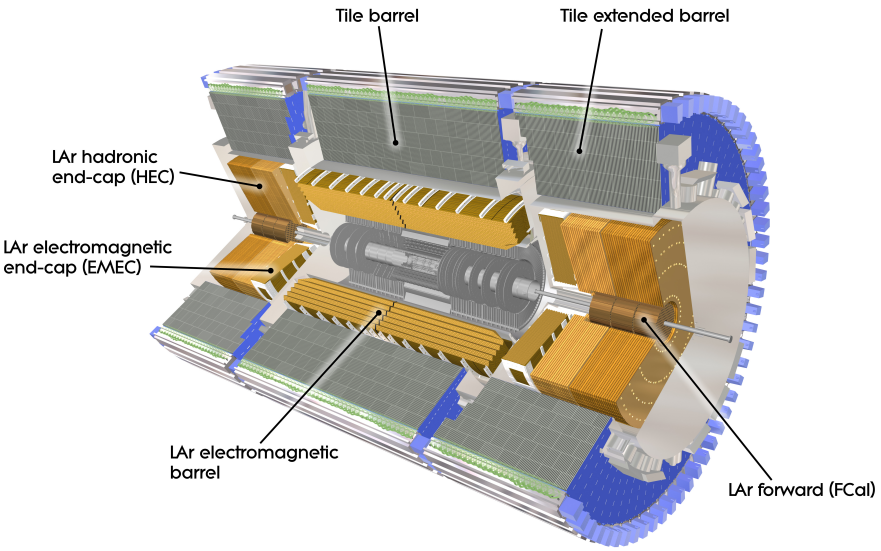

Figure 3.4.: Illustration of the ATLAS calorimeter system with the electromagnetic calorimeter first, followed by the hadronic calorimeter.

and is located in the region $|\eta| < 1.8$.
The hadronic calorimeter detects the strong interaction of hadrons for its measurements. These measurements are already done in the hadronic endcap and forward parts of the LAr calorimeter. The forward calorimeters extend the pseudorapidity range up to $|\eta| < 4.9$ and its modules are capable of measuring both electromagnetic and hadronic interactions. Since the hadronic showers are longer than the electromagnetic showers, another calorimeter is located outside the LAr. The tile hadronic calorimeter covers a pseudorapidity range of $|\eta| < 1.7$ and has a total thickness of 9.7 λ. It is a sampling calorimeter as well but uses scintillating tiles as active material. The passive material is made of steel. The energy resolution of the LAr hadronic endcaps and the tile calorimeter is $50\%/\sqrt{E} \oplus 3\%$ and of the LAr forward calorimeter is $100\%/\sqrt{E} \oplus 10\%$ for hadronic showers.

3.2.4. Muon Spectrometer

In the LHC energy range, muons lose very little energy through Bremsstrahlung while passing through material, therefore an additional detector layer is needed to detect them. The muon spectrometer surrounds the calorimeter and contains separate trigger and tracking chambers. The gas filled tracking chambers are divided into three cylindrical layers around the beam axis and in three layers (endcaps) perpendicular to it. Traversing muons ionise the gas in the chambers, the electrons are accelerated to the anode (wire), which

causes an electron avalanche through further ionisation and generates a current in the wires. The specific configuration of an air-core toroid magnet provides a magnetic field mostly perpendicular to the muon trajectory. The deflection of the muon trajectory due to the Lorentz force allows measurement of the muon's momentum.
For muons with $p_T = 1$ TeV the momentum resolution is $\sigma_{p_T}/p_T = 10\%$. The muon spectrometer covers a range of $|\eta| < 2.7$.

3.2.5. Trigger System

The LHC has a bunch spacing of 25 ns, which leads to a collision rate of 40 MHz. The two-level trigger system that is applied in ATLAS is therefore inevitable to only select and store the interesting events.
The Level-1 trigger (L1) is hardware-based and takes information from the calorimetry system and the muon spectrometer to select events with large energies. The ability to make decisions quickly comes at the expense of the resolution. The L1 reduces the event ratio to 100 kHz.
The second trigger is a High-Level trigger (HLT) and is software-based with fast reconstruction algorithms and uses information not only from the calorimeter and muon chambers, but also from the Inner Detector. This reduces the event rate further to approximately 1 kHz.

4. The $X \to SH \to b\bar{b}q\bar{q}l\nu$ Decay Channel

The decay channel investigated in this thesis is the resonant production of S and H, where the S particle further decays into two W bosons. The BRs of the S boson are assumed to be Higgs boson like. The Higgs boson further decays into a $b\bar{b}$ pair. This decay has the highest BR since both S and H couple to masses as described in subsection 2.4.1. The decay $S \to WW$ has a higher BR than $S \to b\bar{b}$ since m_S is assumed to be larger than $2m_W$ such that both W bosons can be produced on shell. Then one W boson decays hadronically and the other one decays leptonically. The decay is illustrated in Figure 4.1.

4.1. Decay Topologies

As mentioned before, the masses of X and S are not predicted by the theory, so there is a wide range of possible masses, which leads to different decay topologies. The higher the mass difference between the decaying particle and decay products, the smaller the fraction of the event energy going into the masses of the decay products. Therefore, the decay products have a high momentum and have a small opening angle between their direction of flight between their further decay products.
This relation can be obtained in the example of the $H \to b\bar{b}$ decay. In the rest frame of the H boson, the $b\bar{b}$ pair is back to back. This rest frame of the H moves with velocity β with respect to the rest frame of the X particle. Thus, the angle between the $b\bar{b}$ pair is distorted by the Lorentz boost between the two systems. The Lorentz factor is given as the fraction of the energy of the H boson in the lab system and the mass of the H boson, which can be written as follows using energy and momentum conservation

$$\gamma = \frac{\sqrt{(m_X^2 - (m_H + m_S)^2)(m_X^2 - (m_H - m_S)^2)}}{2m_X m_H}. \tag{4.1}$$

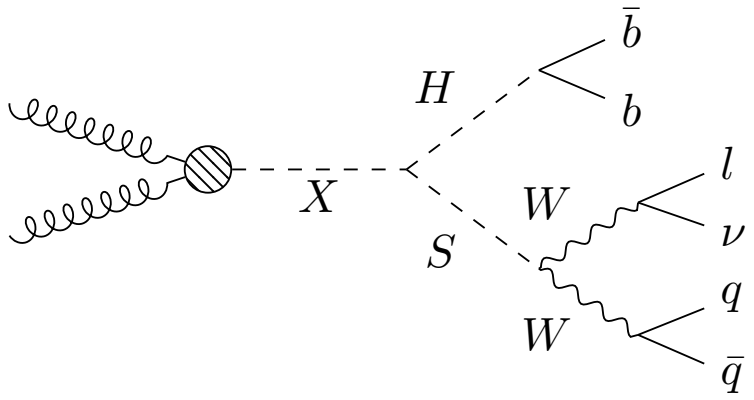

Figure 4.1.: Schematic diagram of the resonant production of the scalar singlet S and the H boson through the resonance X. The H boson further decays into a $b\bar{b}$ pair. The S decays into two W bosons, which then decay hadronically and leptonically.

Thus, the greater the difference between the masses of the H boson, the S and the X particle, the greater γ becomes. The angle between one decay product and the z-axis in the lab system (θ) is related to the angle it has in the rest frame of the H boson (θ^*)

$$\tan(\theta) = \frac{1}{\gamma} \frac{\sin(\theta^*)}{(\cos(\theta^*) + \beta/\beta^*)}, \tag{4.2}$$

where β^* is the velocity of the considered decay product in the rest frame of H. If γ becomes larger, i.e. the mass difference between X and H, then θ becomes smaller. The same applies to the second decay product, so the angle between the direction of flight of both decay products becomes smaller.
If the opening angle between two decay products is small, they are called boosted. The same argument applies for the opposite: if the mass difference is small most of the energy is used to produce the decay products and they have a low momentum. Then the decay products are resolved, meaning there is a wide opening angle in their directions of flight. Regarding the $X \to SH \to bbl\nu qq$ decay, there are various decay topologies depending on the mass distributions of X and S. In this thesis, the mass of H boson is assumed to be $m_H = 125$ GeV. The extreme cases of the topologies are the resolved and the boosted topology, both are illustrated in Figure 4.2. In the resolved decay topology, there is just a small mass difference between X, S and H, so both S and H are produced with a low transverse momentum. All further decay products are then resolved and can be easily reconstructed. For $m_X \leq 1$ TeV and an accordingly small m_S, this decay topology is

dominant. If $m_X \gg m_S, m_H$ the decay has a boosted topology, because much of the event energy is transferred to create large momenta for S and H. This means that all decay products are collimated and the $b\bar{b}$ and $q\bar{q}$ are each reconstructed as a combined object. This decay has a specific topology, that distinguishes signal well from background, but object reconstruction is difficult since tracks are mostly close together. Both extreme cases are not considered in this thesis but help to understand marginal cases in the following topology.

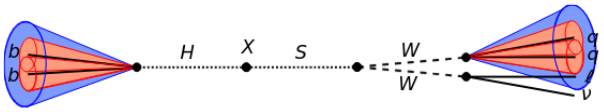

(a)

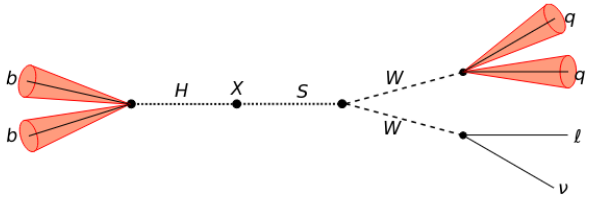

(b)

Figure 4.2.: Illustrations of the (a) boosted and (b) resolved decay topology. In the boosted topology the $b\bar{b}$ and $q\bar{q}$ pair are reconstructed as one jet and the W bosons are boosted too. The decay products in the resolved decay are reconstructed as single objects [51].

4.1.1. Split-Boosted Topology

The topology that is studied in this thesis is the split-boosted topology and is shown in Figure 4.3. This topology occurs if m_X is really large, meaning $m_X \geq 1$ TeV, and m_S is larger than in the boosted decay ($m_S \geq 0.3 m_X$). All samples used in this thesis are generated for combinations of m_X and m_S that fall into the split-boosted topology. The mass points are shown in Section 4.2. Thus, the hadronic decay products of H and one W boson are collimated and are each treated as one large jet. The W boson themselves are separated and the jet from the hadronic decaying W does not overlap with the produced lepton. Thus, the lepton can be reconstructed more accurately than in the boosted topology.

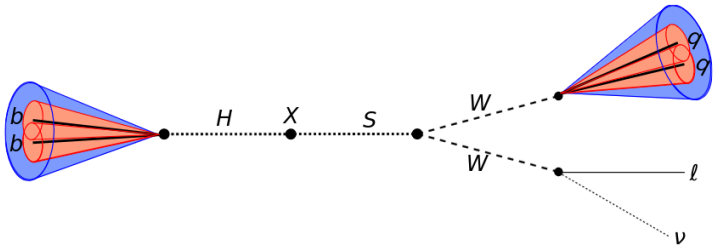

Figure 4.3.: Illustration of the split-boosted decay topology. The $b\bar{b}$ and $q\bar{q}$ pairs are boosted, while the W bosons are resolved [52].

4.2. Monte Carlo Signal Samples

In particle physics not only analyses with real data from particle collisions are performed but Monte Carlo (MC) simulations are used for event generation. This simulation of the data is, especially in decay channels with small cross-sections, very helpful in narrowing the investigated areas of interest. These simulations help in understanding the underlying behaviour, so data can be interpreted correctly.
The Monte Carlo event generation can be roughly divided into three steps. First, the matrix element of the hard scattering is calculated up to a specific order using perturbation theory. After that, the parton showers are simulated, that arise through emission of other quarks and gluons from the partons of the protons and of the decay products. The third step simulates hardronisation, where the partons form bound states. This happens when the particles reach lower energies and perturbation theory is no longer applicable.
The number of generated events in Monte Carlo samples is arbitrary and mostly only depends on the computing power as they are generated. Therefore, the generated events need to be weighted, so that they correctly reflect the yield of expected events. In this thesis, the following equation is used to calculate the expected number of events:

$$N_{exp} = \sigma \cdot \int \mathcal{L} dt \cdot \epsilon \cdot SF_{lep}, \tag{4.3}$$

where σ is the cross-section of the process and is usually provided by a specific model. In this thesis, σ is assumed to be 10 fb.
The luminosity $\mathcal{L}$ describes the number of collisions per area and time, whereas the integrated luminosity is the number of collisions over the time in which the data was taken. For Run 3, the integrated luminosity is estimated to be $\int \mathcal{L} dt = 150$ fb^{-1} in total. Thus, in this thesis, this value is used for the integrated luminosity. The efficiency ϵ is an estimation of the fraction of events that pass the applied selection and can be detected by the experiment. Often in Monte Carlo simulations the events themselves carry a weight to

account for higher-order calculations in the matrix element, which is taken into account in this variable. In addition to that, scale factors, in general, are used to adjust the simulation to the observed data, which are often determined by comparing well-known processes with the simulated data. In this analysis only the scale factors of the lepton, SF_{lep}, are used to account for deviating behavior of the lepton identification algorithms in the MC simulation compared to the behaviour seen in data.
In this analysis Monte Carlo samples, generated for three different mass points, are used. The mass points are the following

1. $m_X = 3000$ GeV, $m_S = 1000$GeV

2. $m_X = 2000$ GeV, $m_S = 1500$ GeV

3. $m_X = 1500$ GeV, $m_S = 750$ GeV

As stated before, the mass difference between X and S affects the topology of this decay. The smaller the mass difference, the less energy can be distributed between the decay products and they are more resolved. Thus, the second sample, that has a small mass difference, is on the edge of split-boosted and split-resolved topologies, where the $b\bar{b}$ pair is resolved, while $S \to WW$ decay appears the same as in the split-boosted topology. A further comparison of all three samples is done in Chapter 6.

5. Object Reconstruction and Event Selection

The signals recorded by the ATLAS detector just include details on the coordinates, the time and occasionally the amplitude of the detected signal, which need to be interpreted. Analysis frameworks employ various algorithms to interpret these signals and assign them to specific particles based on the signatures. Additionally, energy calibrations are required to convert observed detector signals into estimates of the true object energy. This is for example needed because different detector parts can respond differently to passing particles. These procedures are summarised under the term object reconstruction.
The event selection is a set of criteria that are applied to the events to further purify the signal and select events within the split-boosted 1-lepton phase space.
The frameworks, that are compared in this analysis, are the easyjet and SHbbVV frameworks. While the SHbbVV framework only contains code for the analysis of the $X \to SH \to bbVV$ process, the easyjet framework is designed for a wider range of the HH as well as the SH decays, such as the $b\bar{b}b\bar{b}$ final state. In order to be able to discuss the results of the $X \to SH \to bbVV$ analysis from both frameworks, it is necessary to know that they handle events in the same way.

5.1. Lepton and Jet Reconstruction

In proton-proton collisions, one differentiates between prompt and non-prompt leptons. Prompt leptons originate from the decay of heavy bosons or top quarks and are produced shortly after the collision. Thus, they have not traveled far, such that their decay vertex is assumed to be the primary vertex. The leptons decaying from particles that have already traveled a distance in the detector are called non-prompt leptons. In the final state of the split-boosted 1-lepton decay channel, one prompt lepton is present in the final state, which is distinguished into electron or muon since neutrinos cannot be detected directly and τ leptons decay quickly. The leptonically decaying τ is then considered as a prompt electron or muon, whereas hadronically decaying τ leptons are not considered in this anal-

ysis. For the analysis of the one lepton finals state, the distinction between prompt and non-prompt electrons or muons is of crucial importance.
Electrons are identified using energy deposits in the calorimeter and reconstructed tracks in the Inner Detector. The energy deposits are combined in clusters. Reconstruction algorithms then select clusters that are measured in topologically connected areas in the calorimeters. After that the clusters are matched to tracks in the Inner Detector [53]. In addition to that, further selection criteria are applied to all reconstructed lepton candidates for a better selection, which are combined in the terms identification (ID) and isolation. Depending on the requirements on these criteria, various ID and isolation working points (WP) are available that provide different identification and isolation efficiencies and background rejections.
The ID and isolation working points used in this analysis for electrons and muons are adapted to the SHbbVV framework and are shown in Table 5.1.

WP	Muon	Electron
ID	Medium	LooseBLayerLH
Isolation	PflowLooseVarRad	LooseVarRad

Table 5.1.: Working Points (WP) used in this analysis for the electrons and muons.

In order to identify a matched track and cluster as an electron, several discriminating variables are used. They can be found in Table 1 in [53]. The likelihood discriminant

$$d_L = -\frac{1}{15} \ln \left(\frac{L_b}{L_s} \right) \tag{5.1}$$

uses these variables to discriminate prompt electrons from other prompt objects. L_b and L_s are the likelihoods for the reconstructed electron to originate from background (L_b) or signal (L_s). The working points then correspond to a certain threshold above which an object is assumed as electron. In addition to the discriminant, the number of hits in the detector also counts as criteria for the working point. The ID working point used for electrons in this analysis is Loose, but also requires a hit in the innermost pixel layer (LooseBLayerLH).
To differentiate prompt from non-prompt leptons, the isolation variable can be used. It quantifies the activity near the considered lepton from neighbouring tracks. For that, two variables are used, one that sums the p_T of the tracks found within a cone around the electron and one that uses the transverse energy of calorimeter clusters in a given cone. In this analysis the Loose_VarRad working point is used and is defined in Table 5.2. The track variable is built from the scalar sum of the p_T of all tracks inside a cone with a cone

Working Point	Calorimeter	Track	Track p_T^{min}
Loose_VarRad	$topoE_T^{cone20}/p_T^e < 0.2$	$p_{T,LooseCone}^{varcone30}/p_T^{el} < 0.15$	$p_T > 1$ GeV
PflowLoose_VarRad	$(0.4\ E_{T,neflow}^{cone20}/p_T^e + p_{T,LooseCone}^{varcone30})/p_T^{el} < 0.045$		$p_T > 0.5$ GeV

Table 5.2.: Definitions of the isolation working point used in this analysis. Loose_VarRad is the isolation working point for the electron and PflowLoose_VarRad for the muon

size that depends on the transverse momentum of the electron (p_T^e)

$$\Delta R = min\left(\frac{10\text{GeV}}{p_T^e}, 0.3\right) \tag{5.2}$$

Additionally, these tracks fulfill

- $p_T > 1$ GeV
- $|z_0 \sin(\theta)| < 3$ mm
- it has been used in a vertex fit and has the maximum weight or,
- the track has not been used in a vertex fit and $|\Delta z_0 \sin(\theta)| < 5$ mm and $|d_0| < 5$, where $|\Delta z_0 \sin(\theta)|$ is the absolute value of the distance between the z_0 of the track and the primary vertex and $|d_0|$ is the impact parameter with respect to the beam line.

The "LooseCone" tag indicates that tracks associated to the electron and within $|\Delta\eta| < 0.01$ are excluded from the computation of the isolation variable.
The $topoE_T^{cone20}$ variable is the sum of the transverse energy of clusters within a cone of radius $\Delta R = 0.2$ [54].
Since muons interact much less with detector material than electrons, they deposit just minimal energy in the calorimeter system. Therefore, the reconstruction is based on information from tracks in the Inner Detector and the muon spectrometer, as well as energy deposits in the calorimeters [55]. The muon ID used in this analysis is the medium working point. Then, the requirements that muons must pass are: The q/p significance, which is the absolute value of the difference between the ratio of charge and momentum of muons measured in Inner Detector and muon spectrometer, must be smaller than seven. Additionally for tracks at least two precision layers are required. If only one precision layer exists and the track is located in the $|\eta| < 0.1$ region, at most one precision hole layer must be present. A precision layer contains at least three hits in the muon spectrometer and precision holes contain less than three hits and at most three holes.

For the muon, there also is a calorimeter-based and a track-based variable to define its isolation. The working point used in this analysis is the PflowLoose_VarRad and is quantified by the variables as seen in Table 5.2. The track-based variable sums over the p_T of all neighbouring tracks, that fulfill the same requirements as discussed before for the electron, but the p_T threshold is relaxed to 0.5 GeV. The $E_{T,neflow}^{cone20}$ variable is the neutral particle flow energy in a cone around the muon with radius $\Delta R < 0.2$. Neutral indicates that the considered clusters are not associated to tracks.

Since jets are not particles, but are rather defined by grouping hadrons together, their reconstruction is different from the reconstruction of leptons. Because of the hadronization, described in Section 2.1, many hadrons need to be reconstructed and combined into one object, the jet. The algorithm needs to decide which detected particle or energy deposits are assigned to a single jet.
The algorithm used for this analysis is the anti-k_t algorithm [56], which is a Sequential Clustering Algorithm. These types of reconstruction algorithms assume that the transverse momenta of the jet particles have just a small difference and group together particles with similar transverse momenta. The variables used to decide which particles are grouped together are two distances. For the anti-k_t algorithm that is the distance between particles i and j

$$d_{ij} = \min\left(\frac{1}{p_{T,i}^2 p_{T,j}^2}\right) \cdot \frac{R_{ij}^2}{R} \tag{5.3}$$

and the momentum space distance between particle i and the beam axis

$$d_{iB} = \frac{1}{p_{T,i}^2}. \tag{5.4}$$

$p_{T,i}$ is the transverse momentum of the i-th particle. The distance between the two particles in η-ϕ space is $R_{ij}^2 = (\eta_i - \eta_j)^2 + (\phi_i - \phi_j)^2$. The parameter R sets the final size of the jet. This analysis differentiates between small radius jets (SR jets), that have $R = 0.4$ and large radius jets (LR jets) that have $R = 1.0$. The algorithm works roughly as follows: For a list of objects, that are candidates for belonging to a jet, the variables d_{ij} and d_{iB} are computed for each set of objects. If $d_{ij} < d_{iB}$, the particles i and j are combined into one and removed from the list. If d_{iB} is smaller, then particle i is labeled as the jet and is removed and therefore no longer considered in the process. If all objects are assigned to jets the algorithm stops.

5.2. B-tagging

The in this thesis considered decay has a $b\bar{b}$ pair in the final state, so identifying b-jets (jets originating from b-quarks) is crucial to further refine the analysis. B-tagging algorithms exploit the fact that b-hadrons have a relatively long lifetime, resulting in a decay peak of the b-hadron that is displaced from the primary vertex. Also, the large mass of b-hadrons is used to identify b-jets. Due to this large mass, they can decay into many particles with low p_T, which leads to a higher decay product multiplicity than in jets originating from light quarks. Additionally, leptons can be used to identify b-jets since b-hadrons often decay semileptonically. Other reconstructed objects that are used for b-tagging are tracks, which are later matched to the reconstructed jets via their angular distance $\Delta R = \sqrt{\Delta\eta^2 + \Delta\phi^2}$.
There are various b-tagging algorithms used at the ATLAS experiment [57]. For boosted $H \to b\bar{b}$ topologies the b-tagging is extended to $H \to b\bar{b}$-tagging, making use of the same principles. The one used in the easyjet framework is the GN2x tagger. The GN2x tagger is a Graph Neural Network, that takes the jet p_T, jet η and detailed track information of the jets as input and has as output the jet flavour probability. The discriminant used to decide whether the jet is a H_{bb} jet is defined as

$$D_{Hbb} = \ln\left(\frac{p_{Hbb}}{f_{Hcc} \cdot p_{Hcc} + f_{top} \cdot p_{top} + (1 - f_{top} - f_{Hcc}) \cdot p_{qcd}}\right), \tag{5.5}$$

where $p_{Hbb}, p_{Hcc}$and p_{qcd} are the probability scores, that indicate the likelihood of a jet being identified as coming from a $H \to c\bar{c}$ or $H \to b\bar{b}$ decay, a top quark or as a multijet. $f_{Hcc} = 0.02,\ f_{top} = 0.25$ are arbitrary parameters that are used as a compromise between background rejections [58].
The performance of the algorithm is evaluated via working points, that correspond to a specific value of D_{Hbb}. For higher values of D_{Hbb}, the jet is considered as a b-jet. Different working points then correspond to different levels of tagging efficiency and mistag rate.

5.3. W_{had} and H_{bb} Classification

As can be seen in Figure 4.3, in the split-boosted topology the signal contains two LR jets. The decay products of the Higgs boson, the $b\bar{b}$ pair, are reconstructed as a combined jet, which is further called the H_{bb} jet. As well as the $b\bar{b}$ pair, the $q\bar{q}$ pair coming from the W boson is combined as a single LR jet and is called the W_{had} jet. To identify the signal, it is crucial to find these jets. In this thesis, the algorithm to assign the jets as

coming from the H boson or from the W boson boson uses the masses of the signal in an event.

In each event, it is first checked which jet of an event has a mass closest to the mass of the Higgs boson m_H. This jet is then assigned as the H_{bb} jet. From the remaining jets, the jet with a mass closest to the mass of the H boson is assigned as the W_{had} jet. This could also be assigned the other way round, in which case it would first be checked which jet has a mass that is closest to the W boson mass. The remaining jets are then checked to see which jet is closest to the H boson mass.

Depending on whether the H_{bb} or W_{had} jet is classified first in the algorithm, a difference in the distributions of the masses of these jets can be seen, as shown in Figure 5.1 and Figure 5.2. The green distribution is for the sample with mass point (m_X = 3000GeV, m_S = 1000 GeV , further referred to as X3S1), the mass point (m_X = 2000GeV, m_S = 1500 GeV , X2S15) is visualised in red and the blue distribution is from the sample with (m_X = 1500GeV, m_S = 750 GeV , X15S75).

In Figure 5.1 the jet mass distributions of the jets assigned with W_{had} are shown for all three samples. Figure 5.1(a) shows the W_{had} jet masses if the H_{bb} jet is classified first. One can see the peak at the mass of the W boson. But the distribution also peaks at lower jet masses around 10 GeV.

Figure 5.1(b) shows the jet masses of W_{had} if W_{had} is classified first. This distribution also peaks at m_W, but also has slightly more events at m_H. This is reasonable, as both masses are close to each other and if there is no jet that fits the m_W, then the jet with m_H is assigned to W_{had}. The peak around 10 GeV nearly vanishes for this algorithm order.

The situation is similar for the H_{bb} jet mass, which is shown in Figure 5.2. If H_{bb} is classified first (Figure 5.2(a)), one sees a peak at the H boson mass and a smaller one at the W boson mass. Depending on the sample, there can be more or fewer events where $b\bar{b}$ is resolved. The consequence are jets with lower masses than the jet from the combined $b\bar{b}$ quarks. If the H_{bb} jet is classified first and the $b\bar{b}$ pair is resolved, the jet with mass m_W is the nearest to m_H and therefore assigned as the H_{bb} jet. After that the low mass jets (originating from the decay products of the H boson boson if this decay is resolved) are assigned to the W_{had} jet. Thus one can see a peak at m_W for the H boson mass distribution and a peak at smaller jet masses in the W boson mass distribtuion if the H_{bb} jet is classified first.

This happens most for mass points where m_X and m_S are relatively close to each other, as seen in the plots: In Figure 5.1(a), the (m_X = 2000GeV, m_S = 1500 GeV) sample (red) has the highest peaks at small jet masses and in Figure 5.2(a) it has the highest peak at the m_W.

If the W_{had} jet is classified first, the peak in the H_{bb} jet mass distribution at m_W vanishes, but one obtains a peak at the lower jet masses (see Figure 5.2(b)).
From these distributions, it can be concluded that, for this analysis and with the used algorithm, it makes more sense to classify the W_{had} jet first. For this order in the algorithm, the peak in the W_{had} jet mass distribution at m_W is clearer and one has fewer wrongly assigned W bosons to the H_{bb} jets. The small mass jets are then predominantly assigned as H_{bb} jet, which is also more ideal since its decay products are more likely to be resolved than the $q\bar{q}$ pair.

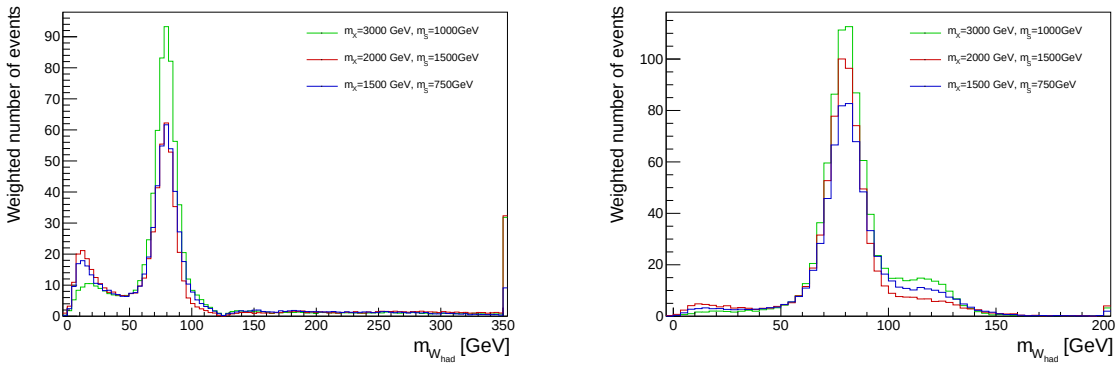

(a) (b)

Figure 5.1.: Mass distributions of the jets assigned to W_{had} for all three mass points. The green distribution is for the $m_X = 3000$GeV, $m_S = 1000$ GeV mass point, the red for the $m_X = 2000$GeV, $m_S = 1500$ GeV and the distribution for $m_X = 1500$GeV, $m_S = 750$ GeV is depicted in blue. The distributions are shown for if H_{bb} (a) or W_{had} (b) is classified first.

5.4. Event Selection

For a robust comparison, both frameworks need to be as harmonized in their event selection as possible. The following object definitions, as well as the event selection, were applied in both analyses. As stated before, the classification of the W_{had} and H_{bb} jets is more advantageous if the W_{had} jet is classified first. However, for this comparison, the analysis uses the algorithm as it was originally implemented and classifies the H_{bb} jet first, such that both frameworks classify the W_{had} and H_{bb} jets in the same way. In addition, jet cleaning, which suppresses noise and pileup in the jet reconstruction, was disabled since this is not present in the SHbbVV framework. However, it should be re-enabled for further analysis in the future.

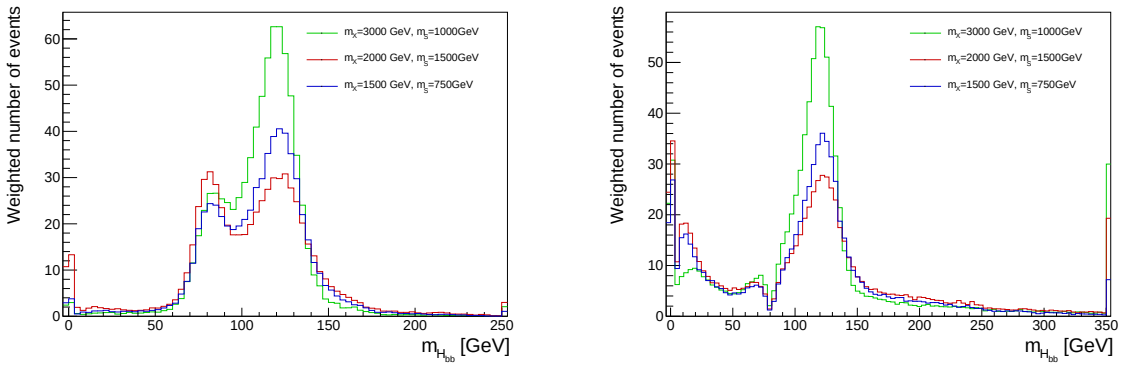

(a) (b)

Figure 5.2.: Mass distributions of the jets assigned to H_{bb} for all three mass points. The green distribution is for the $m_X = 3000$GeV, $m_S = 1000$ GeV mass point, the red for the $m_X = 2000$GeV, $m_S = 1500$ GeV and the distribution for $m_X = 1500$GeV, $m_S = 750$ GeV is depicted in blue. The distributions are shown for if H_{bb} (a) or W_{had} (b) is classified first.

5.4.1. Object Definitions

The following object definitions were applied in both easyjet and SHbbVV framework. The candidates for electrons and muons are required to have a minimum p_T of 10 GeV. Only objects with $|\eta| < 2,47$ for electrons and $|\eta| < 2.5$ for muons are considered. In addition to that electron candidates in the region $\eta \in [1.37, 1.52]$ are rejected. In this area, the barrel overlaps with the top of the end cap, which can lead to poorer reconstruction capabilities, such as incomplete energy measurements.

The requirements for jets are that they fulfill $p_T > 50$ GeV for SR jets and $p_T > 200$ GeV for LR jets. For the LR jet, candidates are considered up for $|\eta| < 2.0$ and SR jet candidates are required to pass $|\eta| < 4.5$.

5.4.2. Overlap Removal

In order to avoid double counting of energy deposits in the detector which are identified as particles, an overlap removal procedure is applied. If more than one reconstructed object is assigned to the same energy deposit, the overlap removal identifies and resolves these ambiguities.
The overlap removal used in this analysis checks for overlapping electrons, muons, SR jets and LR jets. The variable used to quantify the overlap is the angular distance $R = \sqrt{\Delta y^2 + \Delta\phi^2}$, where y is the rapidity. If an overlap is found between muons and

electrons, the electron is removed if the tracks have an angular distance of $R < 0.01$. The overlap between electron and SR jets is resolved by removing the SR jet if the tracks have an angular distance of $R < 0.2$. The same applies to the overlap of muons and jets, but the SR jet is only removed if there are less than three tracks assigned to it. From the remaining SR jets the electron (muon) is removed if the tracks overlap with an angular distance of $R < 0.4$. If an overlap is found between LR jets and electrons, the electron is removed if the tracks have an angular distance of $R < 1.0$. If an overlap is found between SR and LR jets, the SR jet is removed if the tracks have an angular distance of $R < 1.0$. In Figure 5.3, the distributions of number of SR jets of all 3 samples. Figure 5.3(a) shows the distribution with the overlap removal applied, Figure 5.3(b) shows the distribution without the overlap removal for SR jets. It can be seen that in most events there are zero SR jets. As this analysis considers proton-proton collisions with huge QCD backgrounds, one would expect many more SR jets in the event. After further investigations, the issue seemed to be that most of the reconstructed SR jets were removed against the LR jets. A temporary solution to this was found in disabling this part of the overlap removal for the SR jets, although this should not be the final solution since the overlap removal itself is justified. For the expected number of events Equation 4.3 was used with the in Run 3 expected integrated luminosity of $\int \mathcal{L} dt = 150$ fb^{-1} and an assumed signal cross-section of $\sigma = 10$ fb.

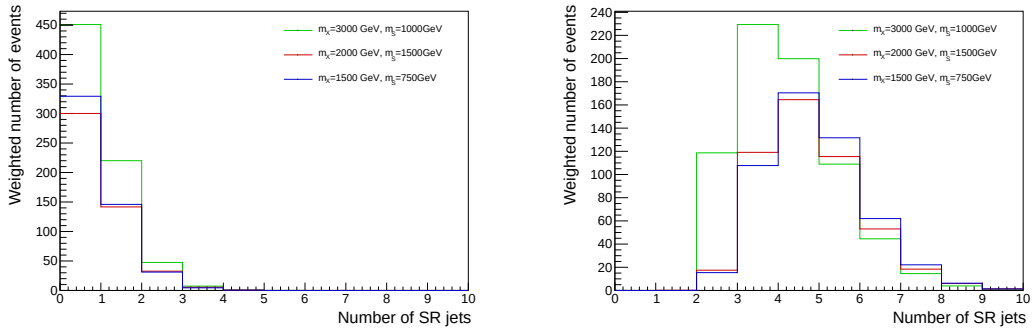

(a) (b)

Figure 5.3.: Expected number of events of the number of SR jets with the overlap removal for the LR jets applied (a) and with the overlap removal disabled (b) for an integrated luminosity of $\mathcal{L} = 150$ fb^{-1} and a signal cross-section of $\sigma = 10$ fb.

5.4.3. Event Selection Criteria

In order to comprehensively assess the experimental results, analyses often use a systematic approach to event selection, which is achieved through the implementation of a series of cuts. These cuts serve as a systematic and hierarchical sequence of selection criteria, applied to the reconstructed events, with each step aimed at enhancing the purity of the selected sample while maintaining a high efficiency. These selection criteria are applied in the same way in both frameworks. In this thesis, the sequence of selection criteria is used to compare the two frameworks quantitatively.
The first selection is made by triggers. As stated in Subsection 3.2.5, triggers are necessary to reduce the amount of information that needs to be evaluated. They select only those events that fulfil loose criteria relevant to the analysis. The triggers used in this analysis are unprescaled single large-R jet trigger without a mass cut that have p_T threshold between 420 GeV and 460 GeV depending on the run period. In addition, single lepton trigger are used. The single electron trigger has p_T threshold between 26 and 140 GeV and the single muon trigger between 24 GeV and 50 GeV depending on the ID of the electron or muon.
After applying the trigger, only events are accepted that contain exactly one lepton since in the considered decay channel only one W boson decays leptonically. Thus, the final state consists of only one lepton. For this cut, the distinction of whether a muon or electron is present is not applied.
From all events with exactly one lepton, only those events are further considered that have at least two LR jets in their final state. Requiring at least two LR jets ensures that all events with exactly two LR jets are included in the analysis while minimizing the probability of unintentionally excluding signal. Setting the requirement to exactly two LR jets might lead to signal loss due to, for example, experimental uncertainties. The one lepton cut is more strict because, among other things, the identification of leptons often has higher efficiencies compared to the jet reconstruction.
From all events that have exactly one lepton and at least two LR jets, only those are further considered that have the split-boosted topology. This is quantified via the angular distance $\Delta R(W_{had}, lep) = \sqrt{\Delta\eta^2 + \Delta\phi^2}$ between the W_{had} jet and the lepton. For the split-boosted topology, the event must satisfy $\Delta R(W_{had}, lep) > 1$, such that there are well-separated W bosons.

5.4.4. Expected Signal Events

The considered decay has a $b\bar{b}$ pair in the final state, so the signal can be further refined by requiring the H_{bb} jet to be b-tagged. This selection criteria was added to those described in Section 5.4.3. Therefore, the b-tagging algorithm described in Section 5.2 was used with a working point of 75%, which corresponds to a value of the discriminant of $D_{Hbb} = 2.735$. For this part of the analysis, only the easyjet framework was taken into account, so the jet cleaning was re-enabled. Additionally, the classification order of the W_{had} and H_{bb} jet classification algorithm was changed compared to the discussion of both frameworks in Section in the following Chapter since Section 5.3 showed that classifying the W_{had} jet before the H_{bb} jet yields more reasonable results.

Figure 5.4 shows the expected number of signal events after each step of the selection

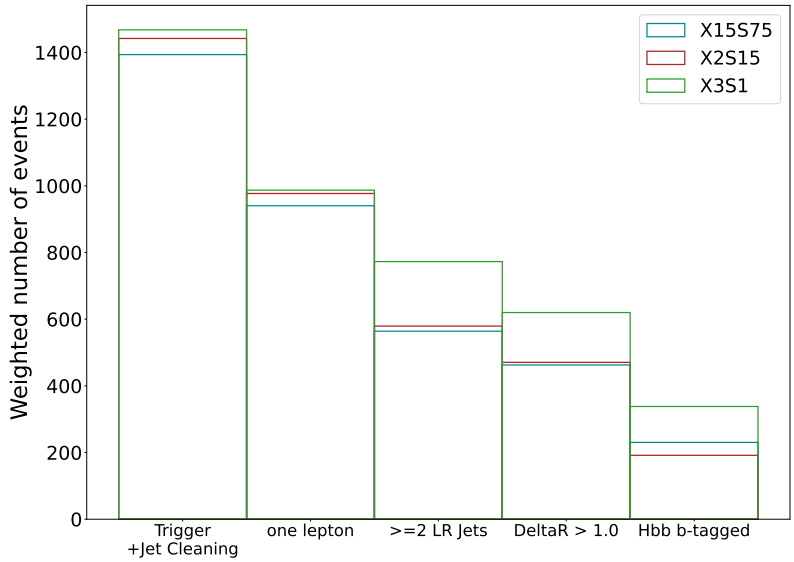

Figure 5.4.: Expected number of signal events for all three samples that remain after each step of the event selection for $\int \mathcal{L}dt = 150$ fb^{-1} and $\sigma = 10$ fb.

criteria for all three samples. The requirement that the H_{bb} jet must be b-tagged is written as "Hbb b-tagged". Table 5.3 shows the MC event yields after all selection criteria are applied, including the "Hbb b-tagged" criterion. The expected number of events are computed using Equation 4.3 with the in Run 3 expected integrated luminosity of $\int \mathcal{L}dt = 150$ fb^{-1} and an assumed signal cross-section of $\sigma = 10$ fb.

From this cutflow it is noticeable that the X3S1 sample yields the most events after each selection criteria, especially after the "$\geq$ 2 LR jets" selection, the number of events

	X3S1	X2S15	X15S75
trigger	1467	1441	1393
= 1-lep	986	977	940
$\geq$ 2 LR jet	772	579	563
$\Delta R(W_{had}, lep) > 1$	619	470	462
Hbb b-tagged	338	191	230

Table 5.3.: Expected number of signal events for all three samples and after each selection criteria for $\int \mathcal{L}dt = 150$ fb^{-1} and $\sigma = 10$ fb.

differs largely between the X3S1 sample and the other two samples. It is also noteworthy that the number of events after the "Hbb b-tagged" selection for the X2S15 sample drops off significantly, whereas the number of events from the X15S75 sample does not decrease as much.

In the following, the distributions of the $\Delta R(W_{had}, lep)$, the p_T and mass of both W_{had} and H_{bb} jets after all selection criteria are applied are shown, to gain further insights in the signal topology of the different mass samples.

The distribution of the $\Delta R(W_{had}, lep)$ variable is shown in Figure 5.5. For the X2S15 sample, most of the events have a higher angular distance between the W_{had} jet and the lepton than in the other samples. Especially in the events from the X3S1 sample the $\Delta R(W_{had}, lep)$ is, for most events, much smaller than for the other two mass points.

The distributions of the W_{had} and H_{bb} jet p_T are shown in Figure 5.6(a) and Figure 5.6(b).

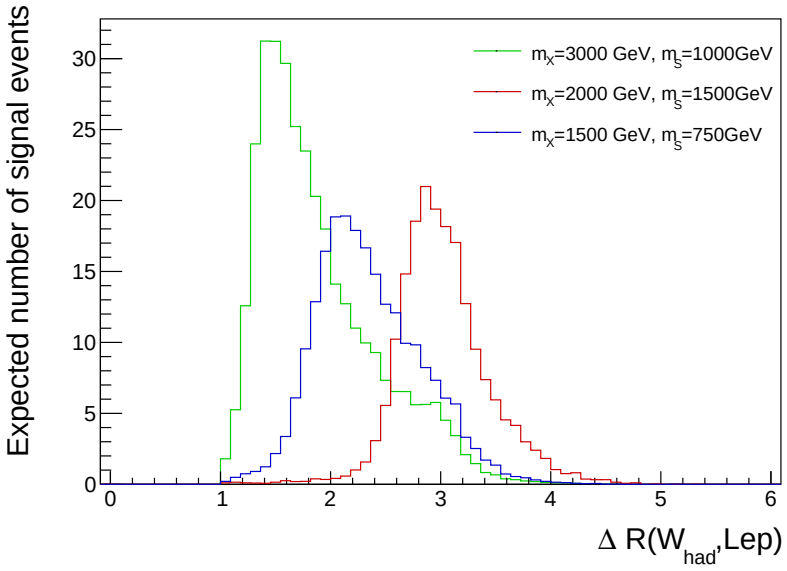

Figure 5.5.: Expected number of signal events of the angular distance between the W_{had} jet and the lepton $\Delta R(W_{had}, lep)$ for all three samples after all selection criteria are applied.

For the X3S1 mass point, the W_{had} and H_{bb} jets have a higher p_T than for the other two mass points. The H_{bb} jets in the X2S15 sample mostly have a slightly lower p_T than the H_{bb} jets in the X15S75 sample. The opposite is true for the W_{had} jets: In the X2S15 sample, they often have a higher p_T than the W_{had} jets from the X15S75 sample.

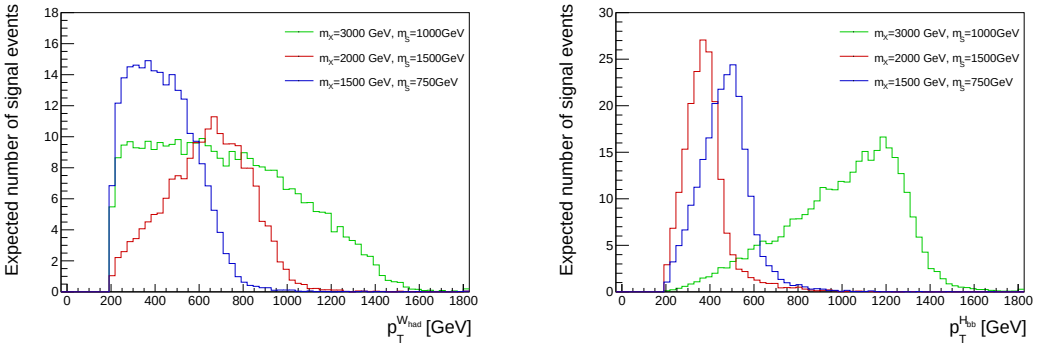

(a) (b)

Figure 5.6.: Expected number of signal events of the W_{had} jet p_T (a) and H_{bb} jet p_T (b) for all three samples after all selection criteria are applied.

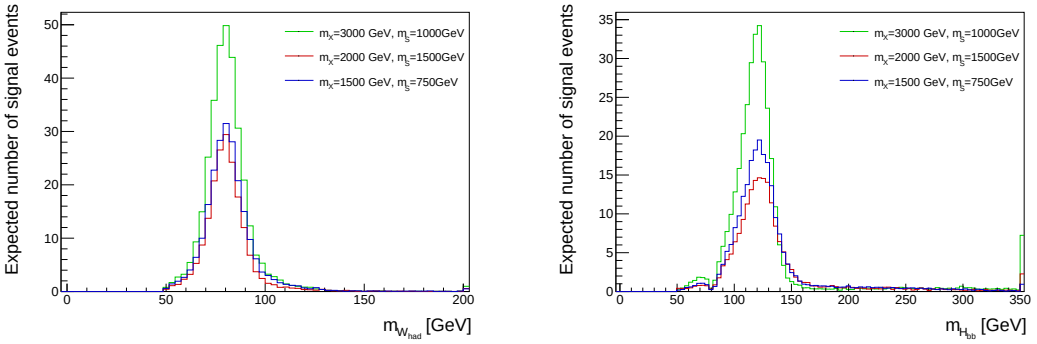

(a) (b)

Figure 5.7.: Expected number of signal events of the W_{had} jet mass (a) and H_{bb} jet mass (b) for all three samples after all selection criteria are applied.

The mass distributions of the W_{had} and H_{bb} jet in Figure 5.7 exhibit a similar shape for all three mass points. The distribution of the W_{had} jet mass features a peak at the mass of the W boson. The H_{bb} jet mass distributions exhibit a peak at the mass of the H boson and a few more events for smaller jet masses. This is consistent with the discussion in Section 5.3.

From this, it can be concluded that the mass point with $m_X = 3000$GeV, $m_S = 1000$ GeV seems to be the sample that fits the requirements for the split-boosted event selection the best since it has the most events left after all selection criteria. Furthermore, the

W_{had} and H_{bb} jets of the X3S1 samples seem to be the most boosted of all samples since, especially for the H_{bb} jet, they have the highest p_T. This is reasonable since it is the mass point with the biggest difference between m_X and m_S, so after producing the H and W boson the most event energy is left that can be used for their p_T. From this, it could have been expected to see the least events in the X2S15 sample after all criteria are applied. The mass difference between X and S is the smallest, such that it can be concluded that this mass point borders the phase space of the split-resolved topology, where the $b\bar{b}$ pair is reconstructed as single objects. Thus, it appears more often in this sample, that an incorrect jet is classified as H_{bb} jet, and thus has a lower chance to be b-tagged than a correctly classified H_{bb} jet.

6. Signal Acceptance Studies

6.1. Event Acceptance for Selection Criteria

In this section, the sequential application of selection criteria based on absolute numbers of the MC simulated events and relative efficiencies are compared. For the relative efficiencies, the event yields of each cut are divided by the event yields of the previous cut. This was done to have a better comparison of each cut at the point in the signal selection where it is applied, because each cut is dependent on previous selection criteria.
For each mass point, the samples contain 100000 events. The MC event yields and relative efficiencies for the sample with mass point ($m_X = 3000$GeV, $m_S = 1000$ GeV , X3S1) are shown in Table 6.1. For the mass point ($m_X = 2000$GeV, $m_S = 1500$ GeV , 2S15) this is depicted in the Table 6.2 and the numbers for the mass point ($m_X = 1500$GeV, $m_S = 750$ GeV , X15S75) are shown in Table 6.3. In order to better visualise this comparison, the absolute numbers and relative efficiencies for all samples are shown in histograms in Figure A.3, A.8 and A.13 in the appendix.

(a)

Sample	X3S1	
Framework	easyjet	SHbbVV
all events	100000	100000
trigger	99496	99498
= 1-lep	64517	65549
$\geq$ 2 LR jet	50470	51725
$\Delta R(W_{had}, lep) > 1$	48598	49850

(b)

Sample	X3S1	
Framework	easyjet	SHbbVV
all events	-	-
trigger	0.99496	0.99498
= 1-lep	0.6484	0.6588
$\geq$ 2 LR jet	0.7823	0.7891
$\Delta R(W_{had}, lep) > 1$	0.9629	0.9638

Table 6.1.: Comparison of the (a) absolute numbers and (b) relative efficiencies from the cutflow made with the easyjet framework and the SHbbVV framework for sample $m_X = 3000$GeV, $m_S = 1000$ GeV .

After applying the trigger, slightly different numbers of events remain in both frameworks. In the easyjet framework, there are fewer events left after applying the trigger than in the SHbbVV framework. This difference is small compared to the total number of events in

(a)

Sample	X2S15	
Framework	easyjet	SHbbVV
all events	100000	100000
trigger	97752	97781
= 1-lep	63132	64314
$\geq$ 2 LR jet	37176	38318
$\Delta R(W_{had}, lep) > 1$	33413	34528

(b)

Sample	X2S15	
Framework	easyjet	SHbbVV
all events	-	-
trigger	0.97752	0.97781
= 1-lep	0.6458	0.6577
$\geq$ 2 LR jet	0.5889	0.5958
$\Delta R(W_{had}, lep) > 1$	0.8988	0.9011

Table 6.2.: Comparison of the (a) absolute numbers and (b) relative efficiencies from the cutflow made with the easyjet framework and the SHbbVV framework for sample $m_X = 2000$GeV, $m_S = 1500$ GeV .

(a)

Sample	X15S75	
Framework	easyjet	SHbbVV
all events	100000	100000
trigger	94534	94581
= 1-lep	61573	62567
$\geq$ 2 LR jet	36747	37643
$\Delta R(W_{had}, lep) > 1$	34859	35748

(b)

Sample	X15S75	
Framework	easyjet	SHbbVV
all events	-	-
trigger	0.94534	0.94581
= 1-lep	0.6513	0.6615
$\geq$ 2 LR jet	0.5968	0.6016
$\Delta R(W_{had}, lep) > 1$	0.9486	0.9497

Table 6.3.: Comparison of the absolute numbers (a) and relative efficiencies (b) from the cutflow made with the easyjet framework and the SHbbVV framework for sample $m_X = 1500$GeV, $m_S = 750$ GeV .

each sample and thus not further investigated in this thesis, although it should be kept in mind, that different triggers or related offline thresholds are applied in both frameworks. The biggest difference can be seen in the criterion "1-lep", for which exactly one lepton needs to be present. After applying this selection, around 1000 events less remain in the easyjet framework than in the SHbbVV framework. The next criterion "$\geq$ 2 LR jet" applied is the requirement of at least two LR jets in the events. After starting from differing numbers on which this selection is applied, the absolute numbers after this selection cannot be expected to fully agree anymore. However, one can see that for this criterion, the relative efficiencies are more similar than for the "1-lep" criterion. This leads to the conclusion that the LR jet selection works more similarly in both frameworks than the selection for exactly one lepton. The last selection "$\Delta R(W_{had}, lep) > 1$" which selects the split-boosted topology also has a comparable relative efficiency for both frameworks, while the absolute numbers still differ.

In order to better compare each cut by itself, the deviations of each cut between both

frameworks are also investigated, which can be seen in Table 6.4. If the cuts after the "1-lep" selection worked similarly in both frameworks, one would not expect any further inconsistencies, i.e. the deviations of MC event yields for the following cuts would not grow. One notices that the deviations after applying the last selection criteria remain approximately constant, so it is suspected that this selection works similarly in both frameworks.
In the "$\geq$ 2 LR jets" selection it is noticeable that in the X2S1 and X15S75 samples the deviations of the MC event yields become less, which could indicate that there might be a deviation in the opposite direction in this selection. Fewer events are then rejected in the easyjet than in the SHbbVV framework.
In the X3S1 sample, the deviation becomes greater as more selection criteria are applied, unlike in the other samples. As the samples undergo exactly the same analysis, this indicates differences in the reconstruction of the objects. The decay products of the signal have different kinematics depending on the mass point, which in turn has an effect on their reconstruction. Differences in the samples can therefore indicate that objects such as leptons and jets are reconstructed differently in both frameworks. Whether analysing different samples has an effect on the differences in efficiency between the cuts in both frameworks is beyond the scope of this thesis and would need investigations of more than three different samples, but it may need to be considered in further studies.

Sample	X3S1	X15S75	X2S15
trigger	2	47	29
= 1-lep	1032	994	1182
$\geq$ 2 LR jets	1255	896	1142
$\Delta R(W_{had}, lep) > 1$	1252	889	1115

Table 6.4.: Deviation of the MC event yields for each selection between both frameworks computed for each mass point.

As can be clearly seen from the tables in Section 6.1, the most problematic event selection is the "1-lep" criterion, which has the largest difference in MC event yields after its application. In addition, the "$\geq$ 2 LR jet" criterion seems to have an effect on the differences between the two frameworks. However, it is difficult to estimate what influence this cut really has or whether it is only strongly influenced by the inconsistency of the "1-lep" selection. In order to investigate the difference in both frameworks further, the distribution of kinematic variables from the leptons and the assigned jets are investigated in the next Section.

6.2. Comparison of the Kinematic Distributions

The distribution of the kinematic variables are compared after all the criteria have been applied on the events since only these numbers are available from the SHbbVV framework. For all mass points, the differences seen in MC event yields between the frameworks seem to be caused by the same effect. Therefore, the comparison of the kinematic distributions will only be described for the sample with the mass point X3S1. As some small differences between the mass points were already visible in the previous section, the most divergent distributions are discussed in subsection 6.2.1. However, all plots were made for all samples and are included in the Appendix A and B.
As the largest inconsistency between the two frameworks is caused by the single lepton criteria, the distributions of the lepton pseudorapidity η and transverse momentum p_T have been plotted for both frameworks. In order to better understand the source of this discrepancy, the leptons were also distinguished between electrons and muons. The comparison of the η and p_T distributions for muons and electrons is shown in Figure 6.1 and Figure 6.2. In addition, the histograms are normalised by their integral, so that the y-axis represents the proportion of events in a given bin, in order to compare only the shape of the distributions. These normalised histograms can be found next to the histograms with the MC event yields.

As expected from Table 6.1, for each muon and electron distribution, the MC event yields from the easyjet framework are generally smaller than the numbers from the SHbbVV framework. Looking at the normalised distributions, one can see that the deviation from the shape of the distributions almost vanishes for the η distributions, but is still visible for the p_T histogram.
From this, one can assume that the observed difference in the "1-lep" selection results from the lepton p_T. This could be explained by a different reconstruction of the leptons in the frameworks, that might come from different energy calibrations. Events then may pass a selection differently depending on the properties of the reconstructed objects. For example, as mentioned in Section 5.1, the isolation of the leptons depends on their p_T.
Any observed differences in the MC event yields of the lepton η may result from deviations in the determination of p_T since the normalised η histograms are in good agreement.
To further investigate the second selection criterion ($\geq$ 2 LR jet), the distributions of the kinematic variables of the W_{had} and H_{bb} jets are examined since these are the jets that must be present in the signal. After the "1-lep" selection, the number of events is already different, so the MC event yields cannot be expected to fully agree. For this reason, this section focuses on normalisations of the histograms to compare the shapes of the distributions. The histograms with the MC event yields can be found in the Appendix B. For

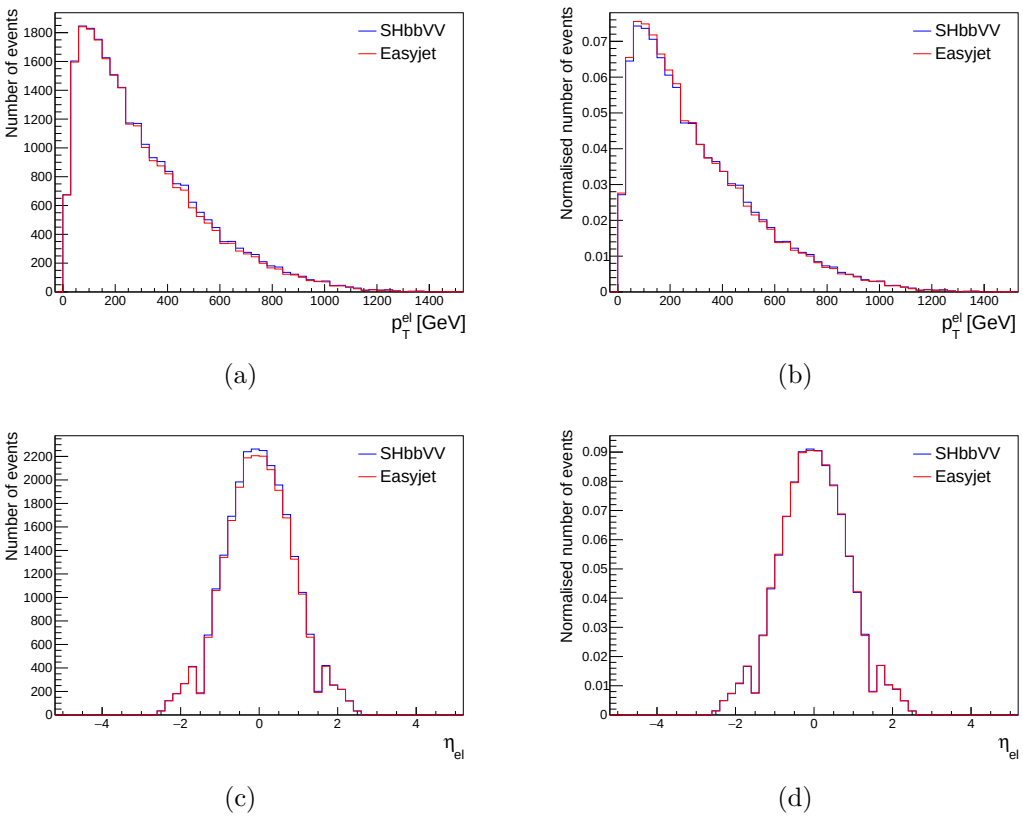

Figure 6.1.: Distributions of the electron p_T (a,b) and η (c,d) after all selection criteria are applied. Numbers from the SHbbVV framework are depicted in blue and from the easyjet framework in red. On the left (a,c) are the MC event yields, whereas the plots on the right (b,d) show the histograms, that were normalised by their integrals in order to compare the shape of both distributions.

the kinematic variables of the W_{had} and H_{bb} jet, a similar trend, as seen in the lepton distributions, is visible: The η distributions of both W_{had} and H_{bb} jets from both frameworks match much better than the p_T distributions. Especially for the W_{had} jet this deviation from the SHbbVV framework is very large as shown in see Figure 6.3(b). The deviation becomes smaller if one considers the H_{bb} p_T distribution as shown in Figure 6.3(a). Generally, the deviation is largest for p_T in the range $[250, 500]$ GeV and for the W_{had} p_T the difference between both frameworks is also visible for p_T up to 1200 GeV. The η distribution and the deviation from the SHbbVV framework do not differ very much for W_{had} and H_{bb} jets. Though the η and mass distributions also do not match perfectly, this seems to be affected by the different selection of jets regarding the p_T, as well as the selection of different events after the "1-lep" selection.

The mass distribution of both the W_{had} and H_{bb} jet are in an even slightly better agree-

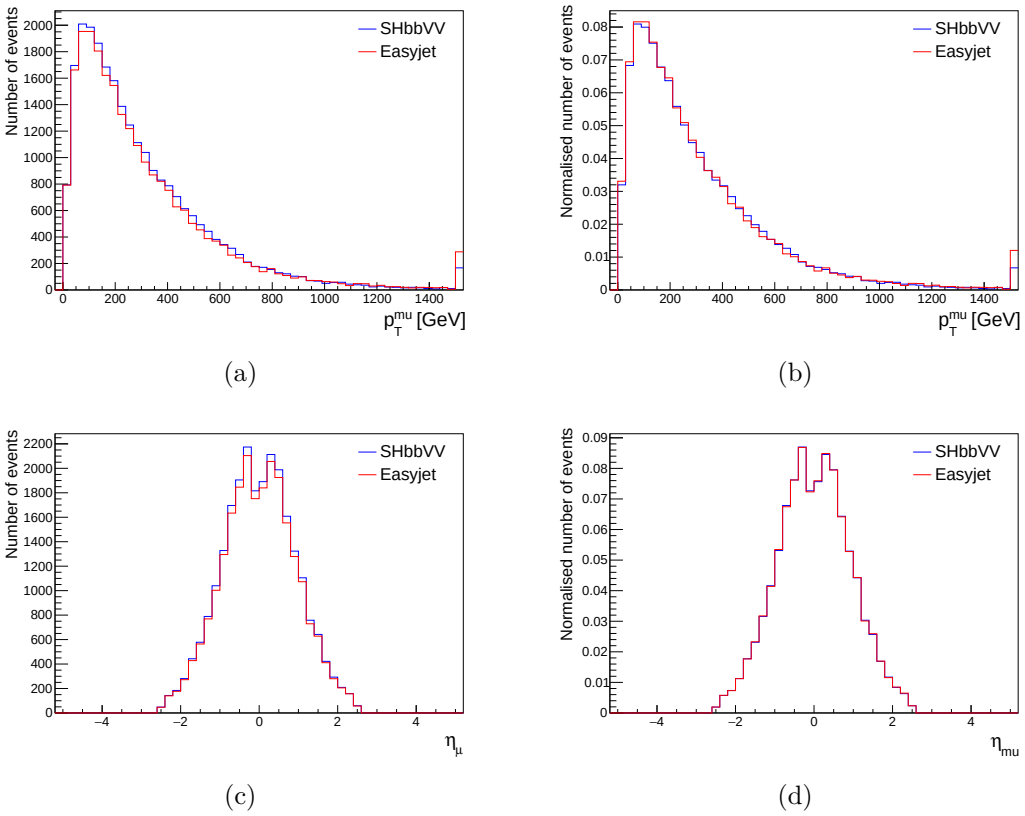

Figure 6.2.: Distributions of the muon p_T (a,b) and η (c,d) after all selection criteria are applied. Distributions from the SHbbVV framework are depicted in blue and from the easyjet framework in red. On the left (a,c) are the absolute numbers, whereas the plots on the right (b,d) show the histograms, that were normalised by their integrals in order to compare the shape of both distributions.

ment with the SHbbVV framework than the η distribution.

Finally, the last selection criteria is further investigated by looking at the distribution of the ΔR between the W_{had} jet and the selected lepton. The comparison of the ΔR distribution for both frameworks is done for the MC event yields in Figure 6.4(a), as well as for the normalised histogram in Figure 6.4(b). As expected from the relative efficiencies in Section 6.1, the normalised distributions of both frameworks are very similar. The differences in the absolute numbers can be explained by the already existing different number of events due to the previous selection.

The general impression from these histograms is that both frameworks do not work similarly regarding the p_T selection of objects. One assumption is that the calibration of the object energy is not done in the same way in both frameworks. Thus, in the preselection, there already is a different definition of the same objects in an event, which might affect

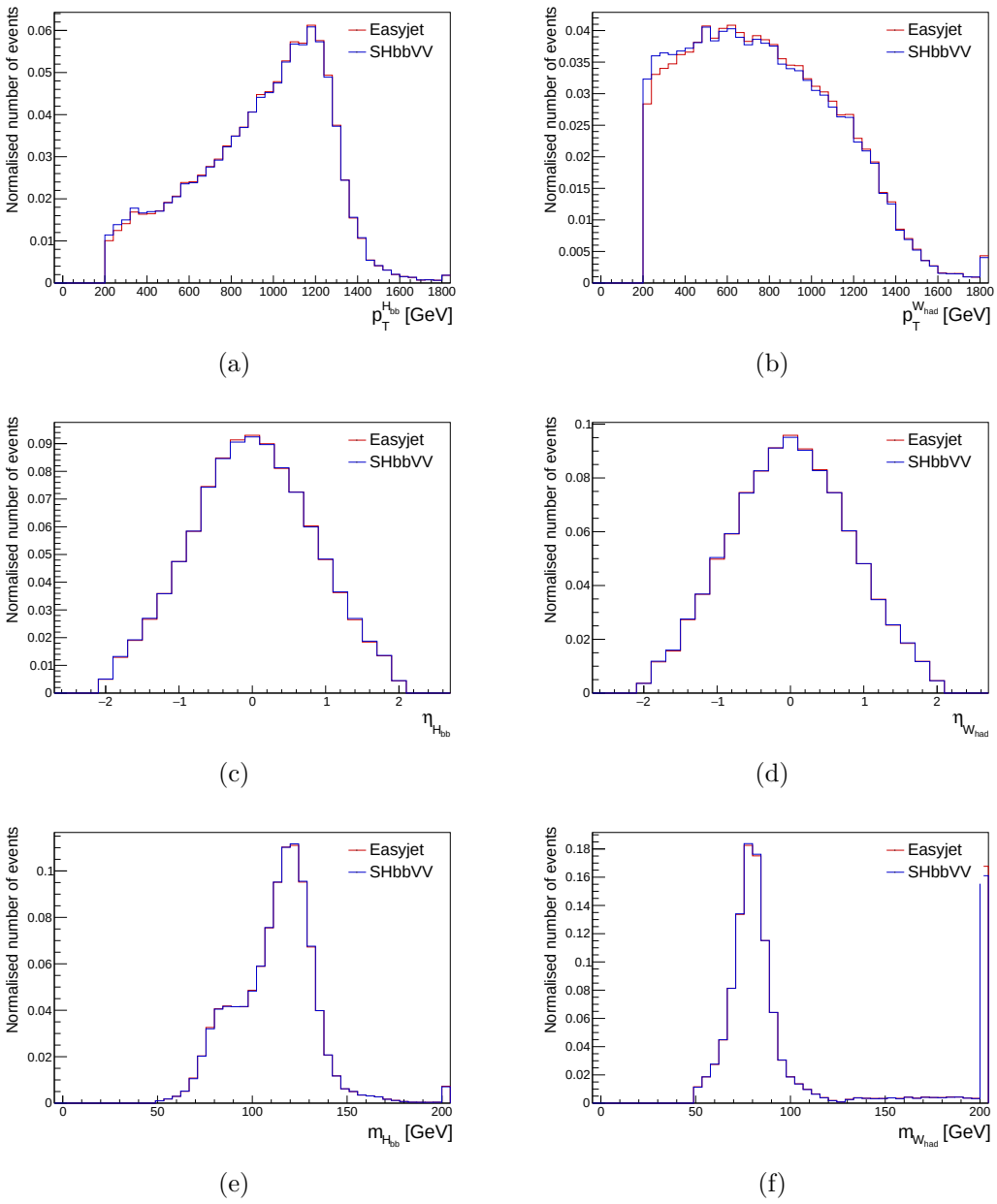

Figure 6.3.: Normalised distributions of the H_{bb} jet p_T (a), η (c) and mass (e). On the right the normalised distributions of the W_{had} jet p_T (b), η (d) and mass (f). The distributions are made after all selection criteria are applied on the events. Distributions from the SHbbVV framework are depicted in blue and from the easyjet framework in red.

the number of these objects in the cutflow. For the LR jet, this different calibration seems not to affect the "$\geq$ 2 LR jets" criterion as much as it does for the "1-lep" criterion since the relative efficiencies of this cut do not differ as much. It might be interesting to observe, how the "$\geq$ 2 LR jets" selection behaves if it is done before the "1-lep" selection.

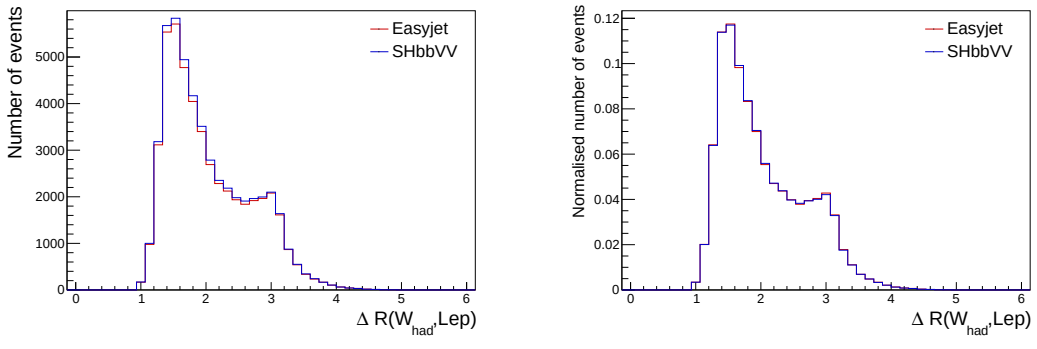

(a) (b)

Figure 6.4.: Distributions of the angular distance ΔR between the W_{had} jet and the lepton. The numbers are made with the SHbbVV (blue) and easyjet (red) framework after all selection criteria are applied. (a) shows the absolute numbers, whereas (b) shows the histogram, that was normalised by the its integral in order to compare the shape of both distributions.

In addition to that the disabled overlap removal could also have an impact on the pre-selection of jets. As can be seen in Section 5.4.2 the overlap removal in this framework removes most of the SR jets against the LR jets and was temporarily disabled. Since the overlap removal is an essential part of the object reconstruction, it should also be taken into account for further investigations.

6.2.1. Differences between the Mass Points

To further investigate the difference in the lepton reconstruction, the number of events with one electron and one muon after applying all selection criteria is investigated. For all samples, the normalised histograms of the number of events with one electron are shown in Figure 6.5. The events are divided into events, where the lepton is an electron (True) and events, where it is not (False). Since only electrons and muons are considered in this analysis, the other bin automatically shows the number of events with exactly one muon. The histograms of the number of events with exactly one muon are thus exactly the opposite and are therefore only included in the appendix in Figure A.2, A.6 and A.11. In Figure 6.5, differences in the normalised histograms especially for the X3S1 mass point are visible. For this sample the normalised number of events that have one muon seem to be exactly the opposite to the SHbbVV framework, the same applies to the number of electrons. In general, it can be seen from Table 6.5 that the absolute number of single muon events deviates more from the SHbbVV framework than the number of single electron events.

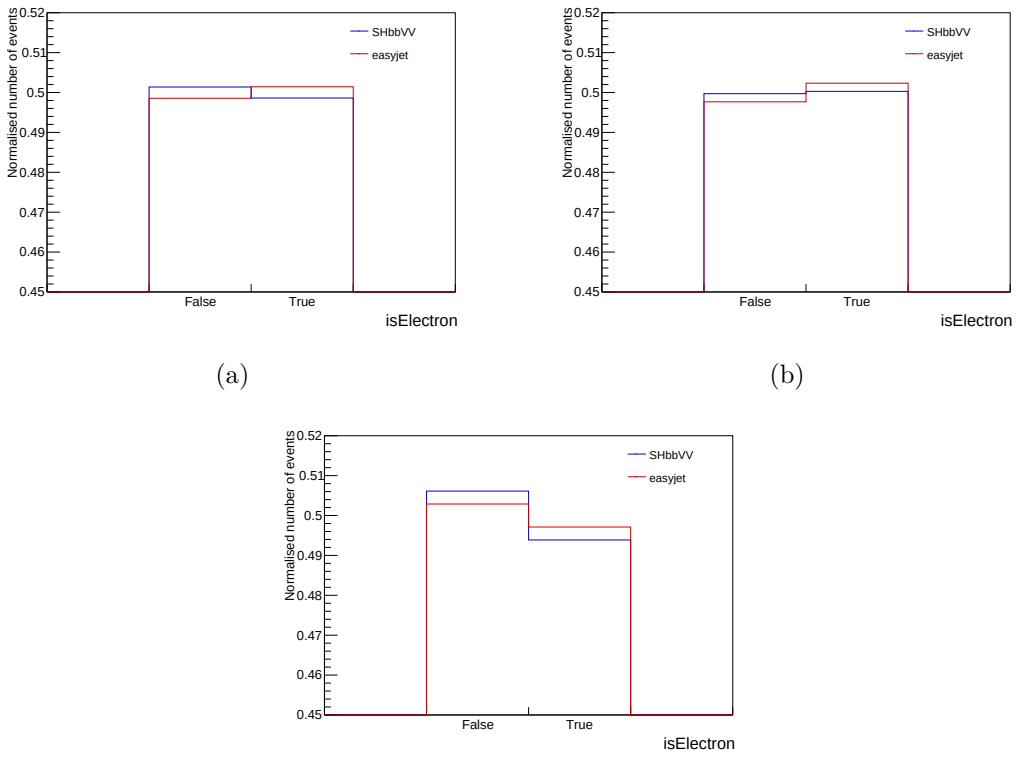

(a)

(b)

(c)

Figure 6.5.: Distributions of the number of events with exactly one electron. The bin "False" contains the events for which the lepton is not an electron (and thus is a muon) and the bin "True" contains the events in which exactly one electron occurs. The distributions from sample X3S1 are shown in figure (a), distribution X2S15 in (b) and X15S75 in (c).

Sample	X3S1		X2S15		X15S75	
Framework	easyjet	SHbbVV	easyjet	SHbbVV	easyjet	SHbbVV
Electron	24368	24856	16785	17274	17329	17655
Muon	24230	24994	16628	17254	17530	18093

Table 6.5.: Comparison of the MC event yields with exactly one electron or one muon after all selections were applied for all samples.

Further differences between the frameworks for different mass points are visible in the p_T distributions of the leptons, and the W_{had} jet variables. Especially for the W_{had} and muon p_T distributions, different deviations between the two frameworks can be seen depending on which sample was used. The distributions of the muon p_T for all samples are compared in Figure 6.6 and for the W_{had} p_T the comparison is shown in Figure 6.7. For the muon p_T distribution, the deviation between the frameworks appears to be greater for the X2S1 sample than for the X3S1 sample.

The opposite is true for the W_{had} p_T distribution. The deviation of the X2S1 sample appears to be somewhat less pronounced. Whether these differences between the samples are systematic or merely coincidental is beyond the scope of this thesis. But, since different masses of the X and S have an impact on the kinematics of the decay and thus on the reconstruction within the analysis, the deviating behaviour of different mass points could be further investigated to obtain clues as to the point at which these inconsistencies in the frameworks occur.

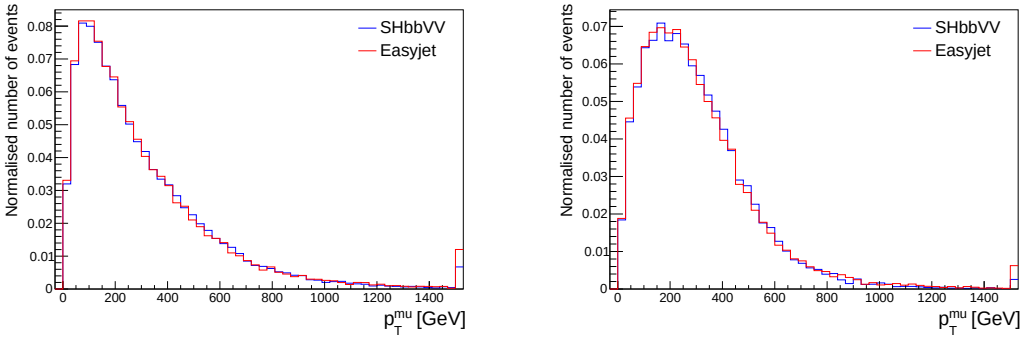

(a) (b)

Figure 6.6.: Distributions of the muon p_T for the samples with $m_X = 3000$GeV, $m_S = 1000$ GeV (a) and $m_X = 2000$GeV, $m_S = 1500$ GeV (b).

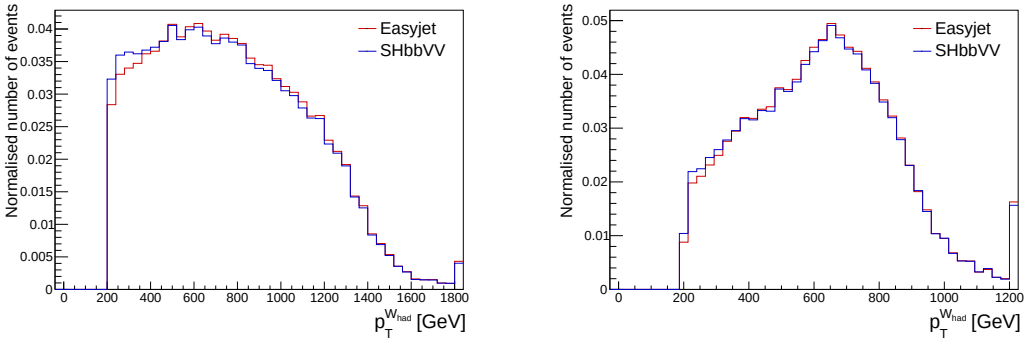

(a) (b)

Figure 6.7.: Distributions of the W_{had} p_T for the samples with $m_X = 3000$GeV, $m_S = 1000$ GeV (a) and $m_X = 2000$GeV, $m_S = 1500$ GeV (b).

7. Conclusion and Outlook

In summary, the easyjet and SHbbVV framework deliver comparable results. The total number of MC events remaining, after all selection criteria were applied, differs from 900 to roughly 1250, which is about one percent of all the events in the sample and about three percent of the remaining events after applying the selection. Just considering the relative efficiencies, the "ΔR" selection is similar for both frameworks and the "$\geq$ 2 LR jet" selection exhibits a good agreement and provides a more consistent result than the "1-lep" selection. Especially after requiring exactly one lepton in the sample, the numbers deviate, although the same events have been used in both frameworks.
Comparing the kinematic distributions of leptons and classified jets, one notices that the distributions with the largest deviation between the frameworks are the p_T distributions. A possible reason for these deviations could be a different calibration of the energies of the leptons and jets in both frameworks, because it affects the object reconstruction. The observed difference in the number of events with one electron or one muon between both frameworks in Figure 6.5 supports this assumption.
Thus it would be interesting to see, whether the results for the "$\geq$ 2 LR jet" selection would be different if this selection is done before the "1-lep" selection. Trying this may provide insight into deviations between the frameworks regarding the jet reconstrution and selection. It might be that the seen deviations in the following selections are mainly caused by already selecting different events in the first "1-lep" selection. Analysing the impact of different cut orders on event yields and distributions can help disentangle the contributions from different stages of the analysis.
In addition, it could provide important insights if the distributions shown in Section 6.2 are examined again without applied selections in order to be able to further investigate these differences in preselection and energy calibration with all generated events.
Furthermore, disabling the overlap removal for the LR jets in one framework can cause deviations. If there are different objects removed due to the overlap removal, this can affect the number of events that pass the "$\geq$ 2 LR jet" selection.
Due to limited analysis time in this thesis, the focus was not on differences seen in the numbers and distributions for different mass points. However, as the mass points affect

the topology and kinematics of the considered decay and therefore the reconstruction of each object, further investigation of the differences between the samples could give a hint, which part of the object reconstruction is inconsistent for the two different frameworks.

The extended Higgs sector is a promising approach in the search for BSM particles and the $SH \rightarrow bbWW$ decay channel has various decay topologies which can be exploited in the event selection. Thus, with regard to the Run3 analysis of the $SH \rightarrow bbWW$ decay channels, it will be important to have both frameworks consistent so that it can be ensured that the results of the easyjet and SHbbVV frameworks are comparable and a common basis for discussion is created. Furthermore, if it is known that both frameworks work in the same way in terms of object reconstruction and event selection, in-depth analyses including background samples and systematic uncertainties could be used to analyse which framework provides the better expected significance.
All in all, the frameworks already deliver comparable results, even if there are differences especially in the reconstruction of the leptons and presumably also the jets. The adaption of these objects and a more detailed investigation of the overlap removal should be an important step towards further harmonisation of the two frameworks.

A. Distributions with normalised number of events

A.1. X3S1 mass point

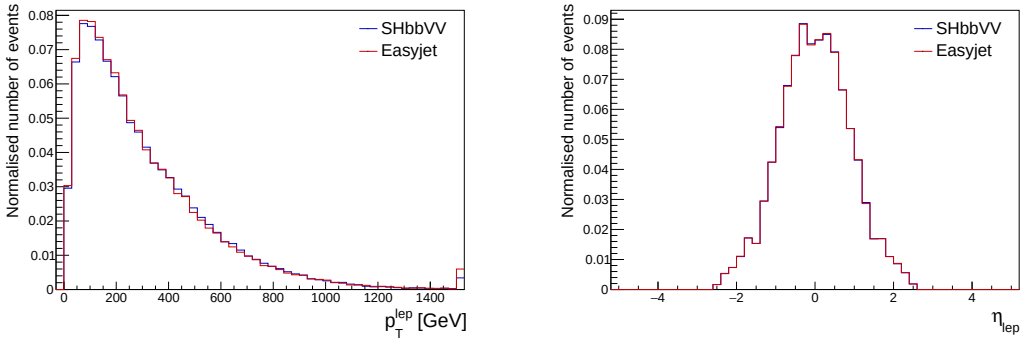

(a) (b)

Figure A.1.: Normalised distributions of the lepton p_T (a) and η (b) from the sample with $m_X = 3000$GeV, $m_S = 1000$ GeV after all selection criteria are applied. The distributions from the SHbbVV framework are depicted in blue and from the easyjet framework in red.

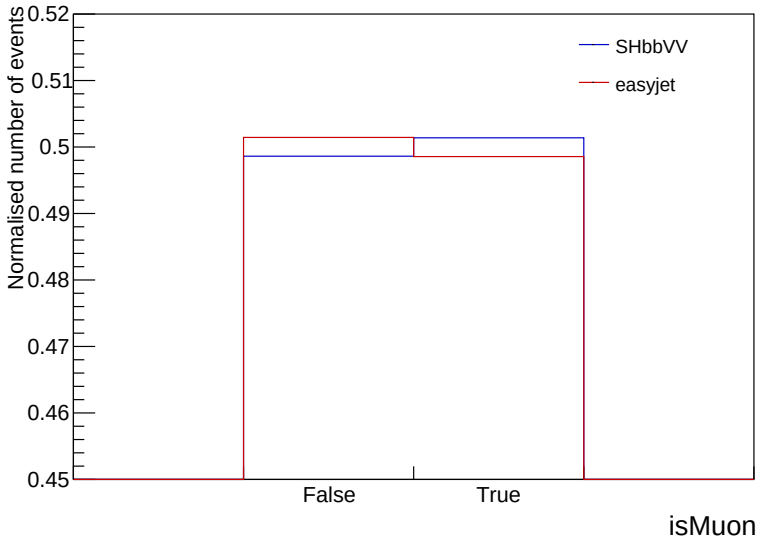

Figure A.2.: Normalised distributions of the number of events with exactly one muon for the sample with $m_X = 3000$GeV, $m_S = 1000$ GeV . The bin "False" contains the events for which the lepton is nota muon (and thus is an electron) and the bin "True" contains the events in which exactly one muon occurs. All selection criteria are applied. Numbers from the SHbbVV framework are depicted in blue and from the easyjet framework in red.

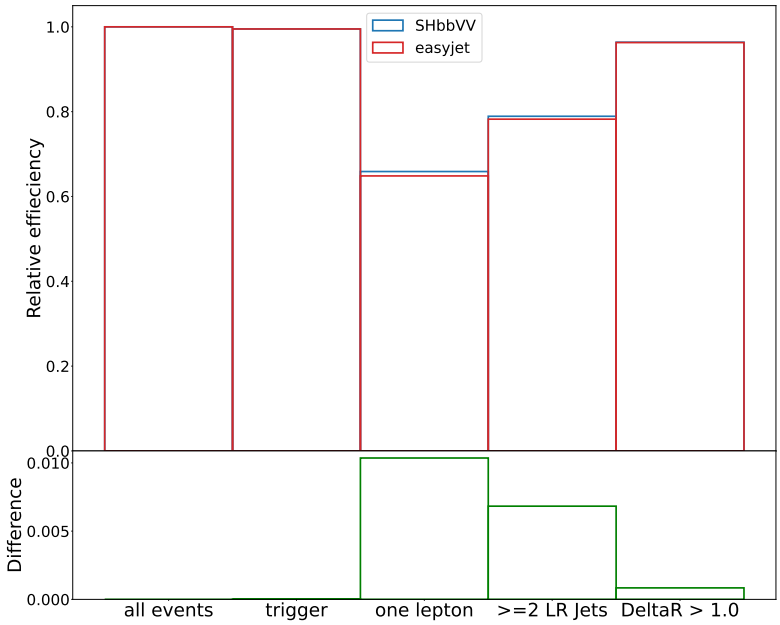

Figure A.3.: Comparison of the histograms of the relative efficiencies from the cutflow for the sample with $m_X = 3000$GeV, $m_S = 1000$ GeV . The numbers from the easyjet framework are depicted in red and from the SHbbVV framework are depicted in blue. The differences between the relative efficiencies is shown in green below.

A.2. X2S15 mass point

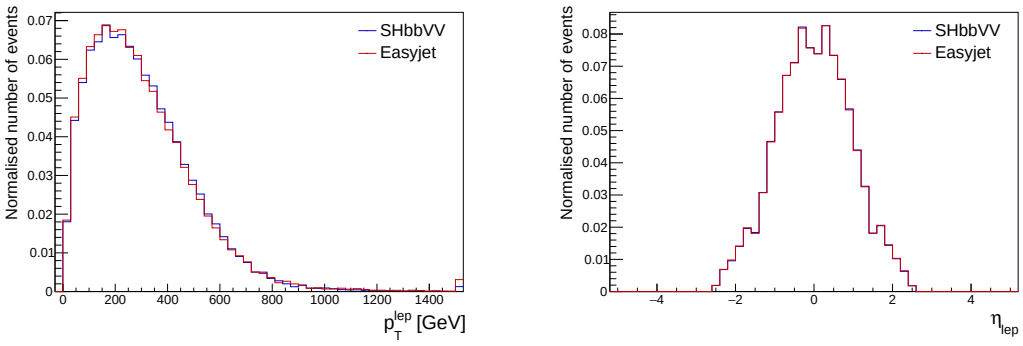

(a) (b)

Figure A.4.: Normalised distributions of the lepton p_T (a) and η (b) from the sample with $m_X = 2000$GeV, $m_S = 1500$ GeV after all selection criteria are applied. The distributions from the SHbbVV framework is depicted in blue and from the easyjet framework in red.

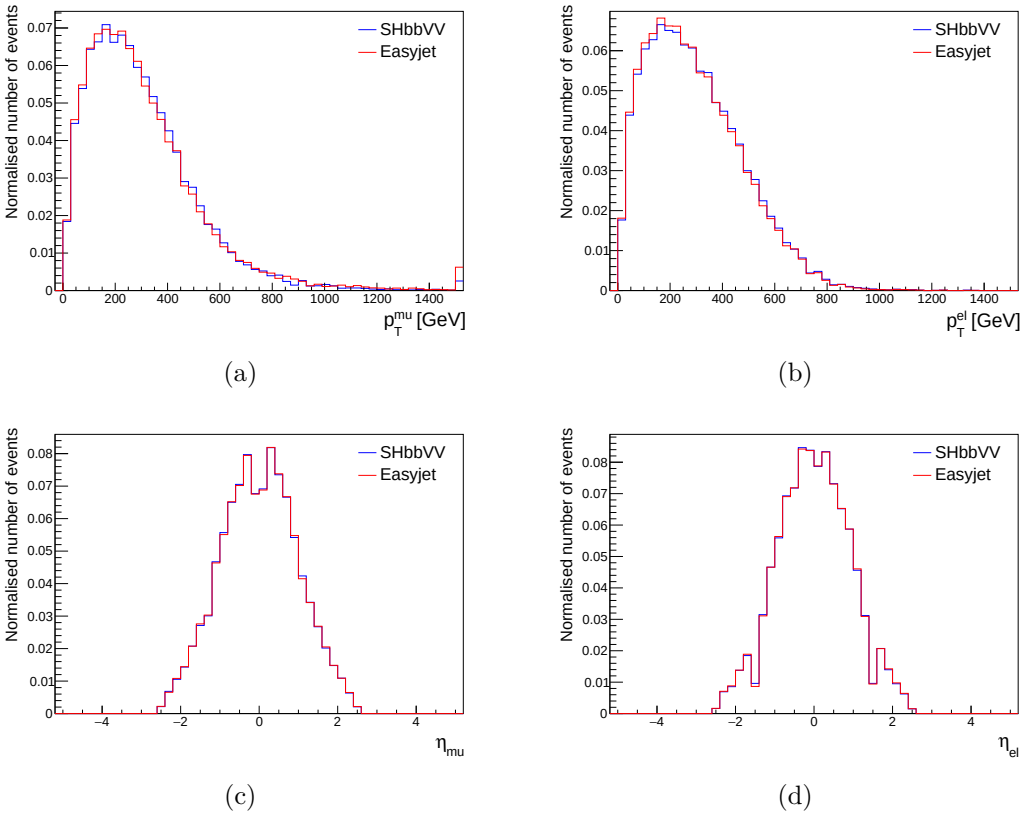

Figure A.5.: Normalised distributions of the muon p_T (a) and η (c), as well as electron p_T (b) and η (d) for the sample with $m_X = 2000$GeV, $m_S = 1500$ GeV . All selection criteria are applied. Numbers from the SHbbVV framework are depicted in blue and from the easyjet framework in red.

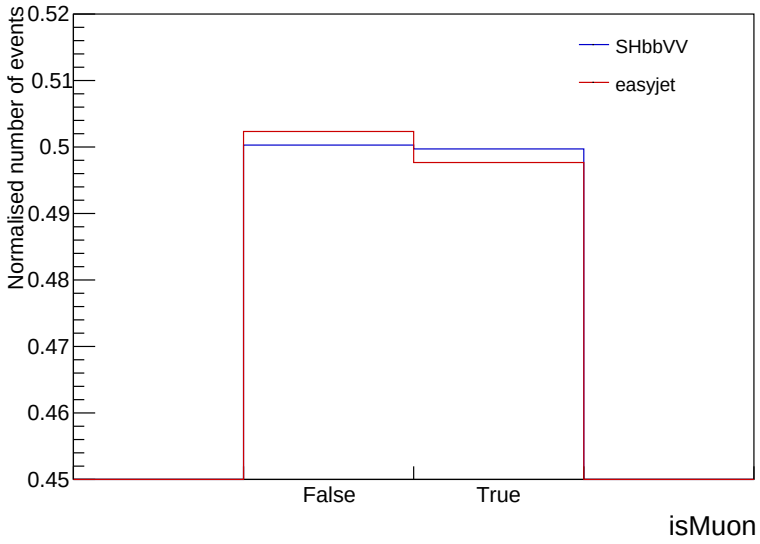

Figure A.6.: Normalised distributions of the number of events with exactly one muon for the sample with $m_X = 2000$GeV, $m_S = 1500$ GeV . The bin "False" contains the events for which the lepton is nota muon (and thus is an electron) and the bin "True" contains the events in which exactly one muon occurs. All selection criteria are applied. Numbers from the SHbbVV framework are depicted in blue and from the easyjet framework in red.

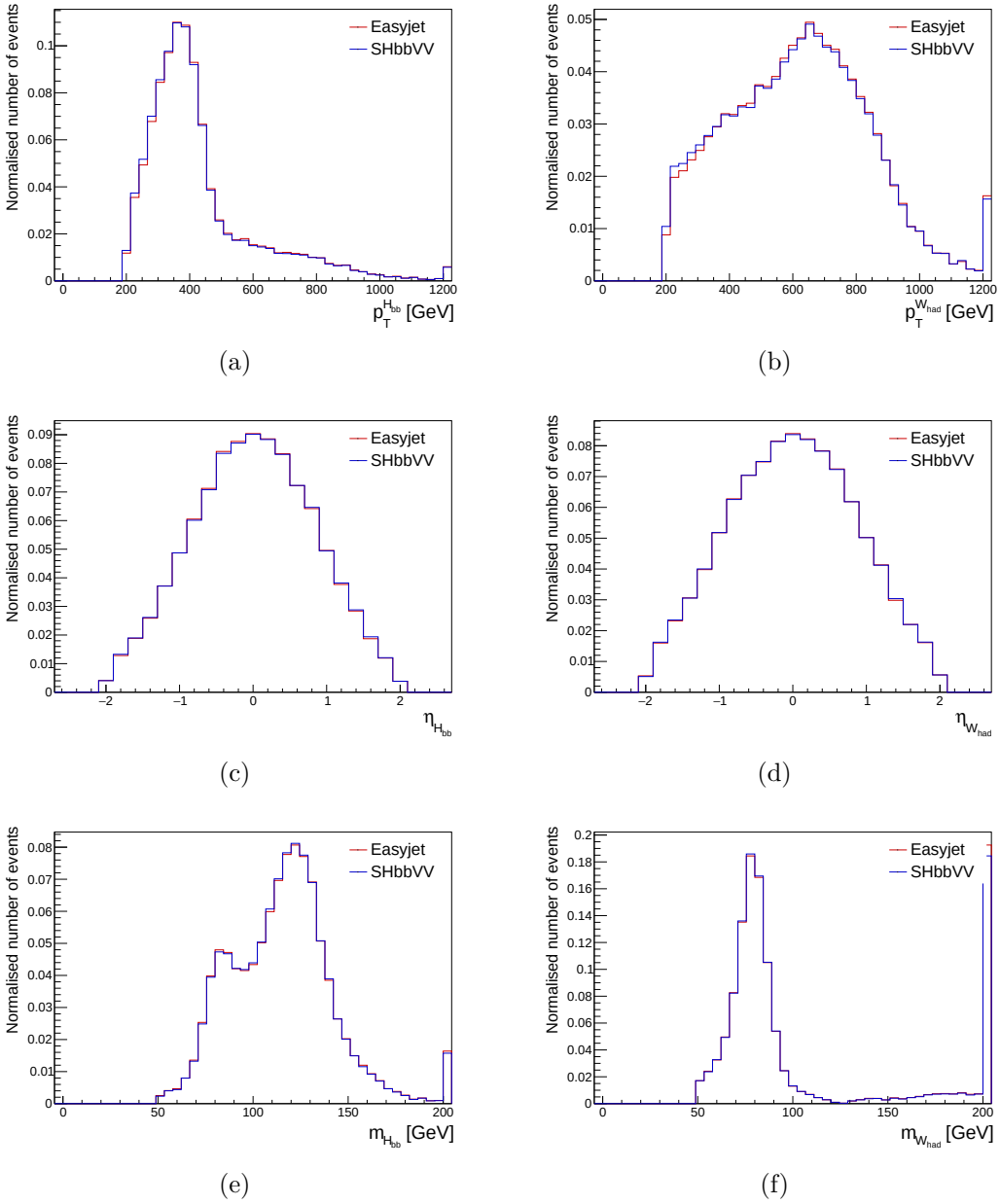

Figure A.7.: Normalised distributions of the H_{bb} jet p_T (a), η (c) and mass (e) and W_{had} jet p_T (b), η (d) and mass (f) for the $m_X = 2000$GeV, $m_S = 1500$ GeV mass point. The distributions are made after all selection criteria are applied on the events. Numbers from the SHbbVV framework are depicted in blue and from the easyjet framework in red.

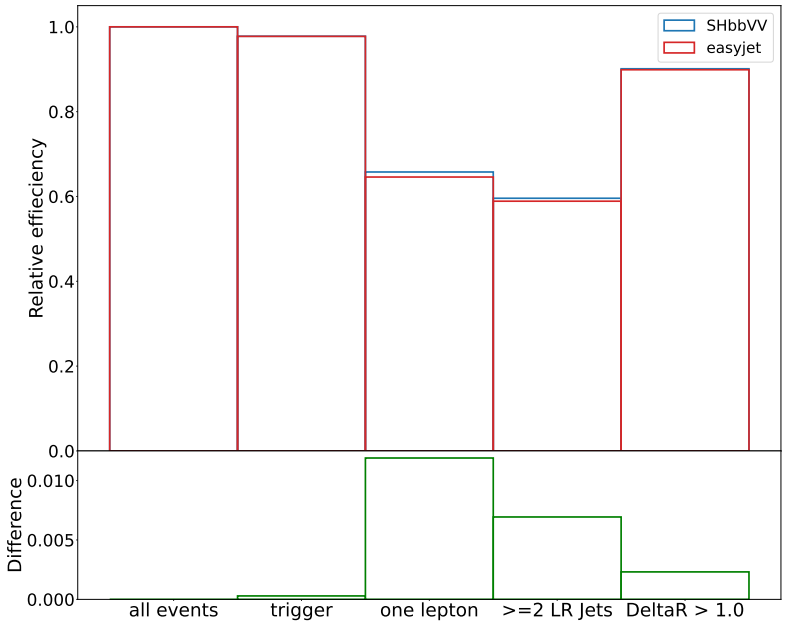

Figure A.8.: Comparison of the histograms of the relative efficiencies from the cutflow for the sample with $m_X = 2000$GeV, $m_S = 1500$ GeV . The numbers from the easyjet framework are depicted in red and from the SHbbVV framework are depicted in blue. The differences between the relative efficiencies is shown in green below.

A.3. X15S75 mass point

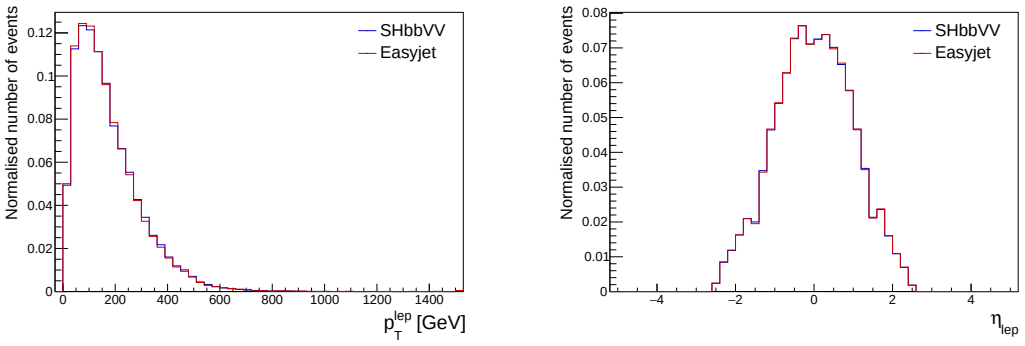

(a) (b)

Figure A.9.: Normalised distributions of the lepton p_T (a) and η (b) from the sample with $m_X = 1500$GeV, $m_S = 750$ GeV after all selection criteria are applied. The distributions from the SHbbVV framework are depicted in blue and from the easyjet framework in red.

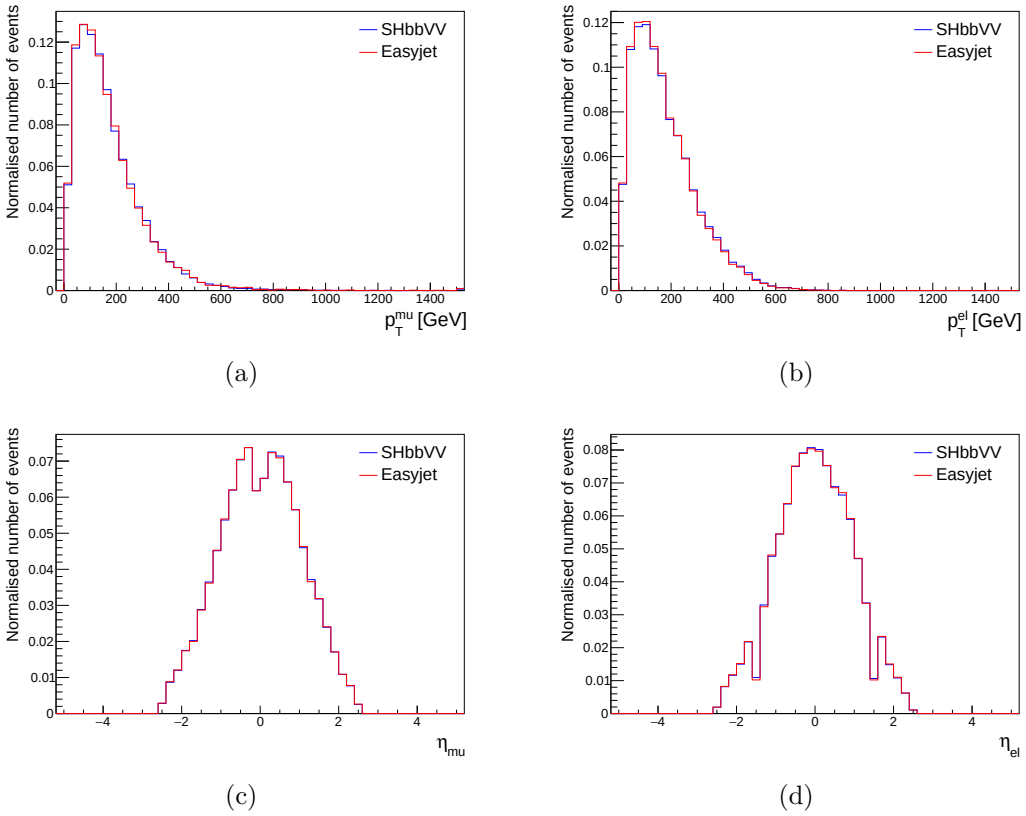

Figure A.10.: Normalised distributions of the muon p_T (a) and η (c), as well as electron p_T (b) and η (d) for the sample with $m_X = 1500$GeV, $m_S = 750$ GeV . All selection criteria are applied. Numbers from the SHbbVV framework are depicted in blue and from the easyjet framework in red.

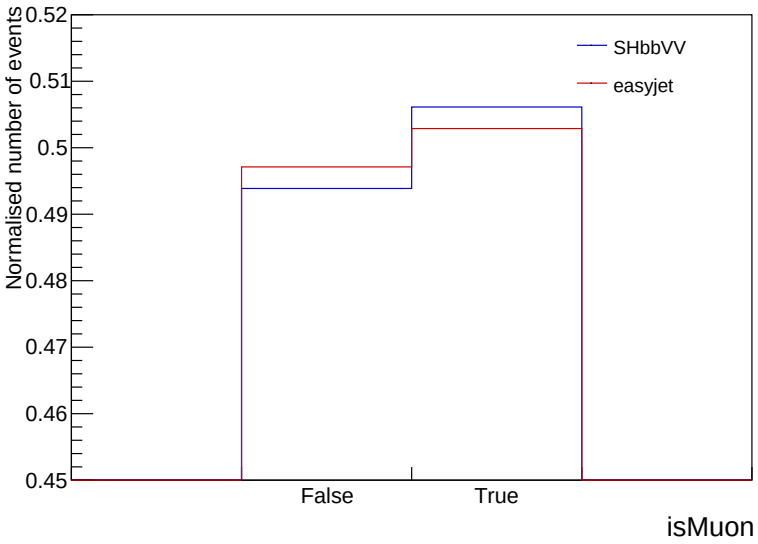

Figure A.11.: Normalised distributions of the number of events with exactly one muon for the sample with $m_X = 1500$GeV, $m_S = 750$ GeV . The bin "False" contains the events for which the lepton is nota muon (and thus is an electron) and the bin "True" contains the events in which exactly one muon occurs. All selection criteria are applied. Numbers from the SHbbVV framework are depicted in blue and from the easyjet framework in red.

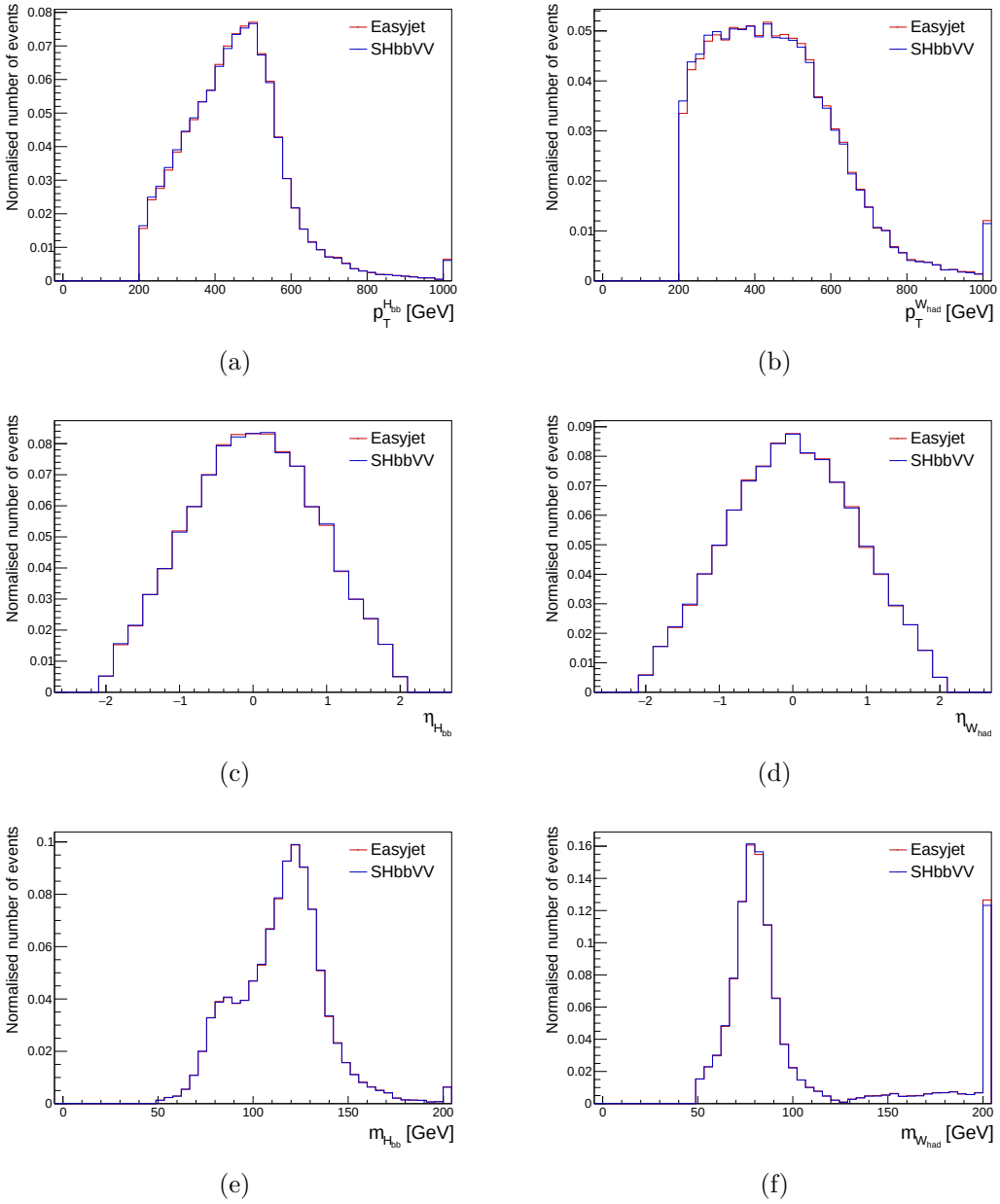

Figure A.12.: Normalised distributions of the H_{bb} jet p_T (a), η (c) and mass (e) and W_{had} jet p_T (b), η (d) and mass (f) for the $m_X = 1500$GeV, $m_S = 750$ GeV mass point. The distributions are made after all selection criteria are applied on the events. Numbers from the SHbbVV framework are depicted in blue and from the easyjet framework in red.

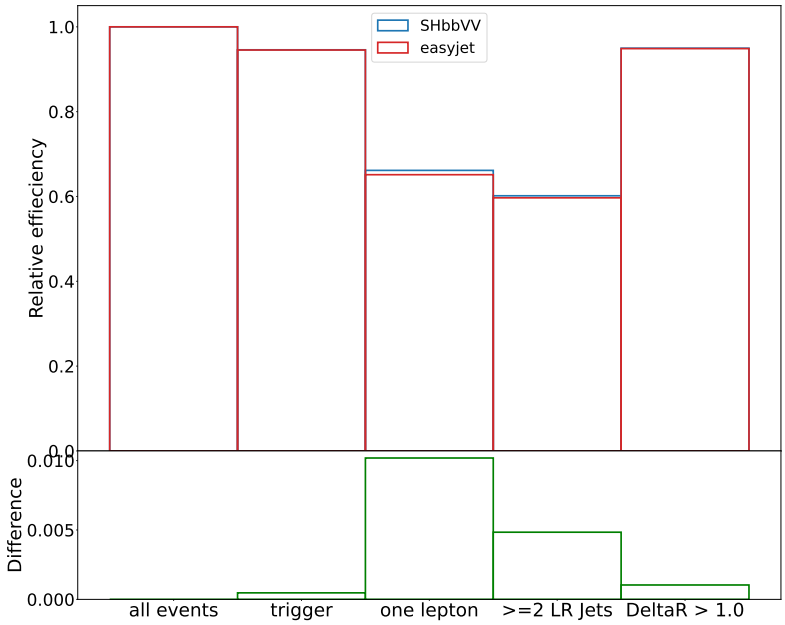

Figure A.13.: Comparison of the histograms of the relative efficiencies from the cutflow for the sample with $m_X = 1500$GeV, $m_S = 750$ GeV . The numbers from the easyjet framework are depicted in red and from the SHbbVV framework are depicted in blue. The differences between the relative efficiencies is shown in green below.

B. Distributions with absolute number of events

B.1. X3S1 mass point

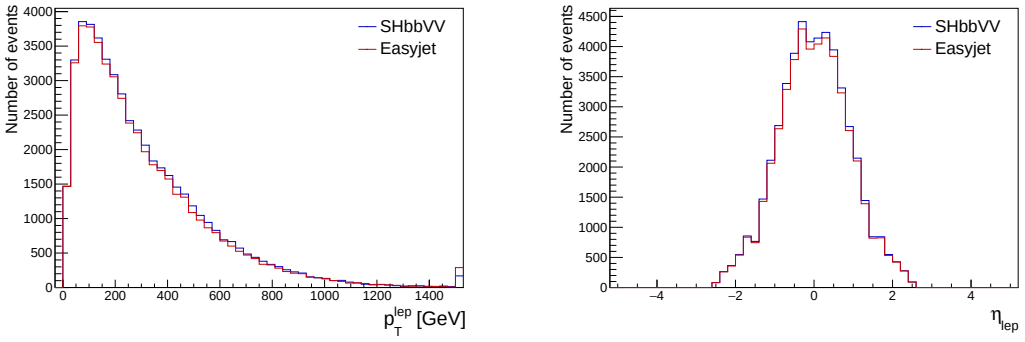

(a) (b)

Figure B.1.: Distributions of the lepton p_T (a) and η (b) from the sample with $m_X = 3000$GeV, $m_S = 1000$ GeV after all selection criteria are applied. The distributions from the SHbbVV framework are depicted in blue and from the easyjet framework in red.

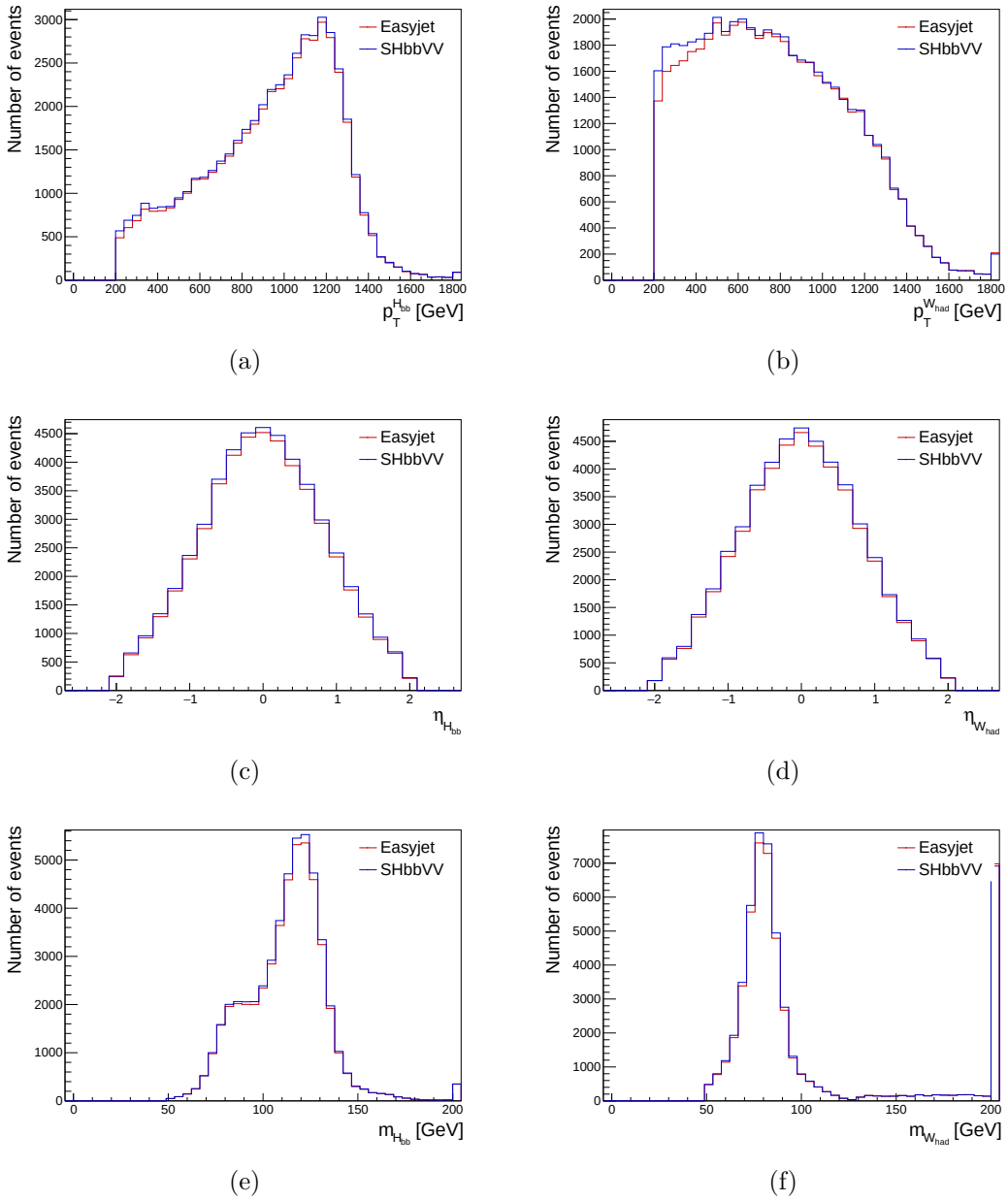

Figure B.2.: Distributions of the H_{bb} jet p_T (a), η (c) and mass (e) and W_{had} jet p_T (b), η (d) and mass (f) for the $m_X = 3000$GeV, $m_S = 1000$ GeV mass point. The distributions are made after all selection criteria are applied on the events. Numbers from the SHbbVV framework are depicted in blue and from the easyjet framework in red.

B.2. X2S15 Mass Point

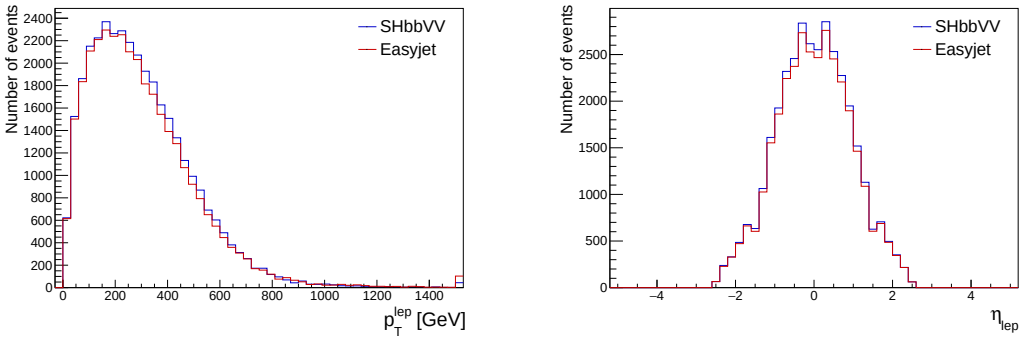

(a) (b)

Figure B.3.: Distributions of the lepton p_T (a) and η (b) from the sample with $m_X = 2000$GeV, $m_S = 1500$ GeV after all selection criteria are applied. The distributions from the SHbbVV framework are depicted in blue and from the easyjet framework in red.

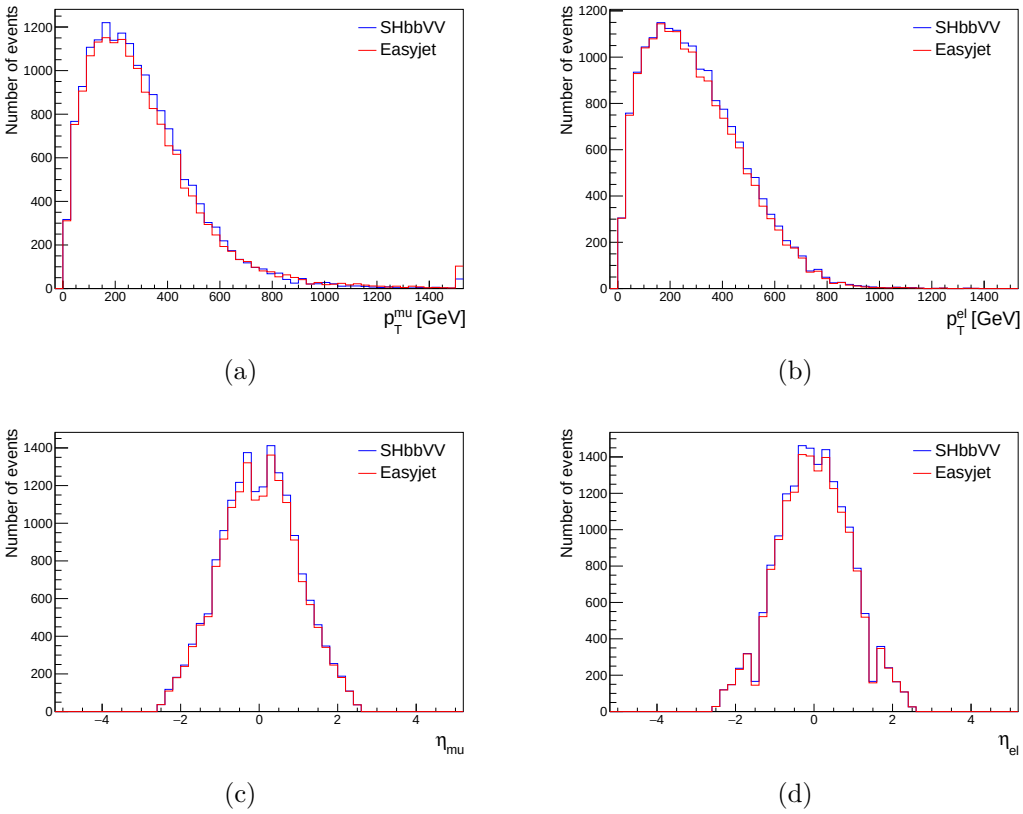

Figure B.4.: Distributions of the muon p_T (a) and η (c), as well as electron p_T (b) and η (d) for the sample with $m_X = 2000$GeV, $m_S = 1500$ GeV . All selection criteria are applied. Numbers from the SHbbVV framework are depicted in blue and from the easyjet framework in red.

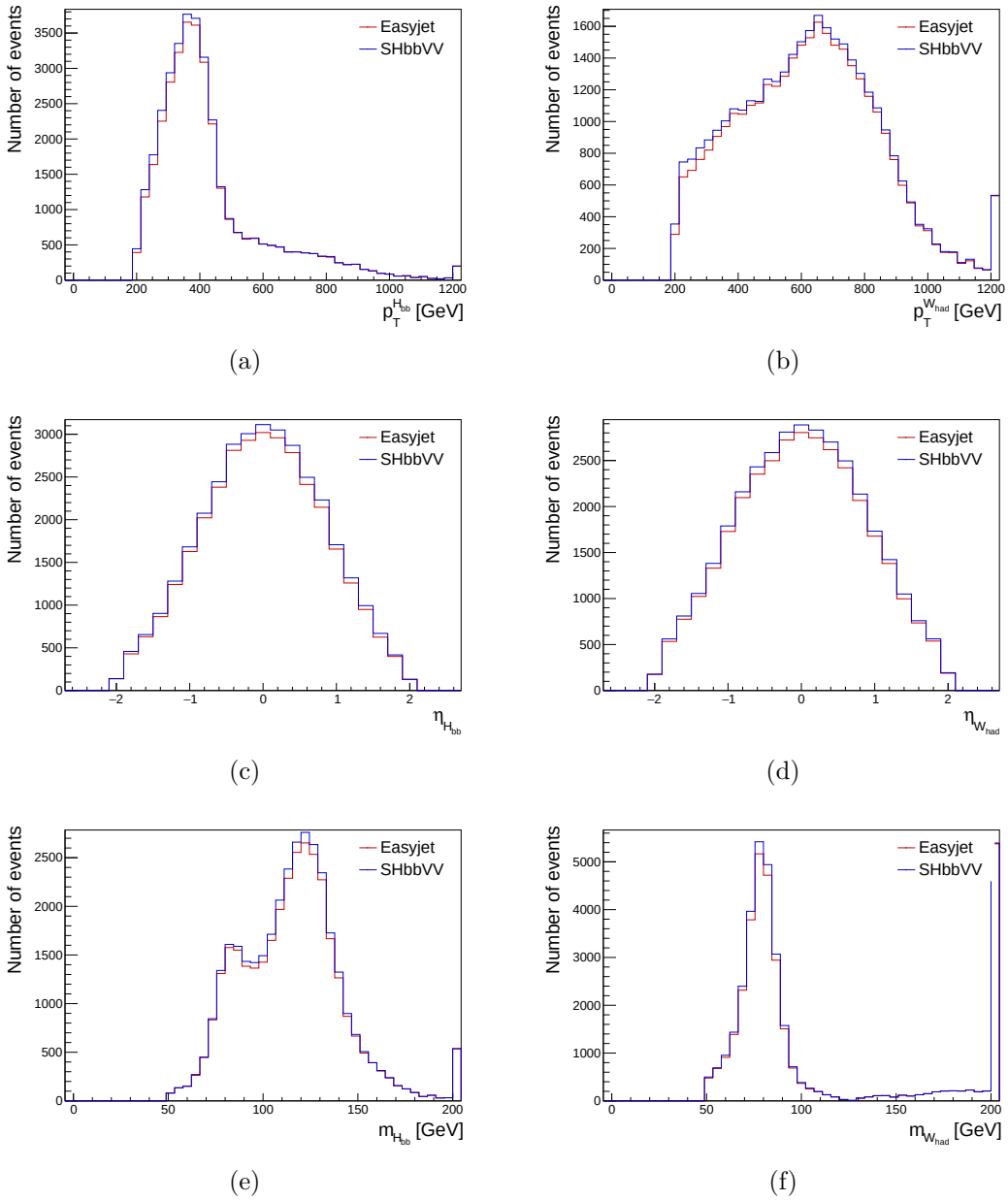

Figure B.5.: Distributions of the H_{bb} jet p_T (a), η (c) and mass (e) and W_{had} jet p_T (b), η (d) and mass (f) for the $m_X = 2000$GeV, $m_S = 1500$ GeV mass point. The distributions are made after all selection criteria are applied on the events. Numbers from the SHbbVV framework are depicted in blue and from the easyjet framework in red.

B.3. X15S75 Mass Point

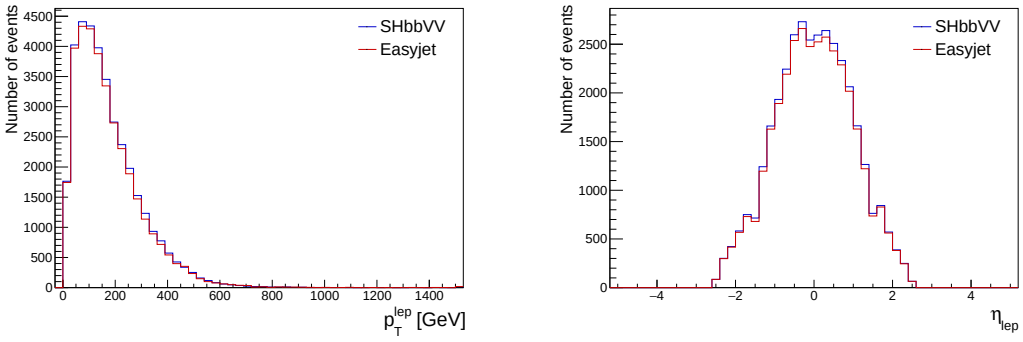

(a) (b)

Figure B.6.: Distributions of the lepton p_T (a) and η (b) from the sample with $m_X = 1500$GeV, $m_S = 750$ GeV after all selection criteria are applied. The distributions from the SHbbVV framework are depicted in blue and from the easyjet framework in red.

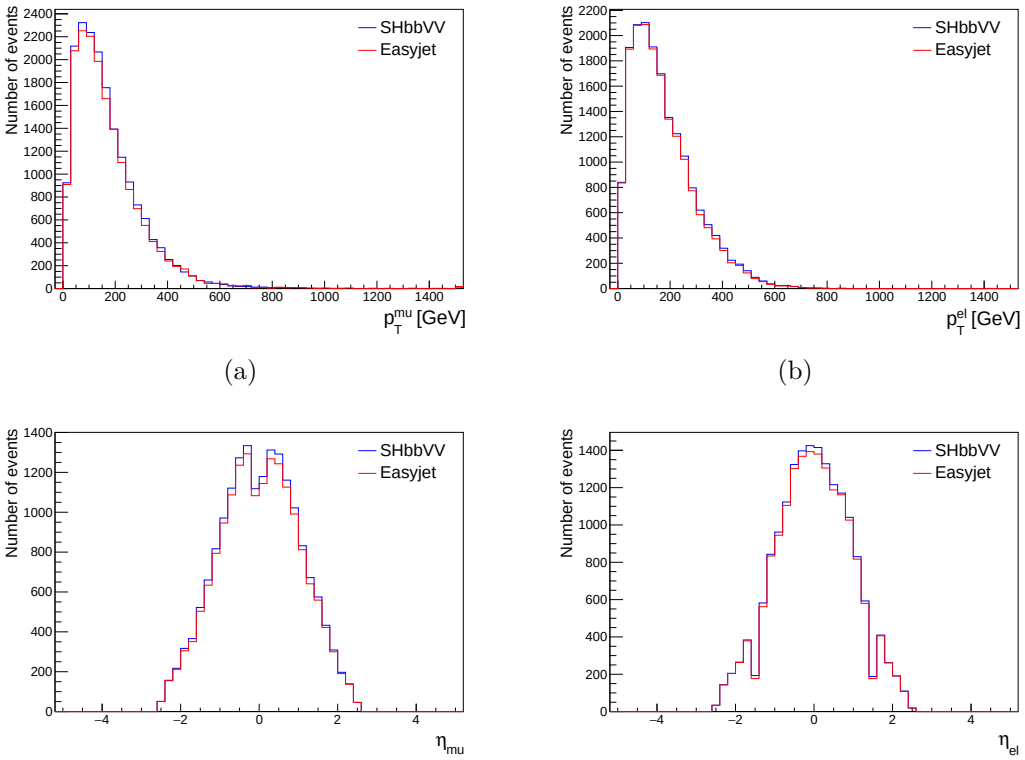

Figure B.7.: Distributions of the muon p_T (a) and η (c), as well as electron p_T (b) and η (d) for the sample with $m_X = 1500$GeV, $m_S = 750$ GeV . All selection criteria are applied. Numbers from the SHbbVV framework are depicted in blue and from the easyjet framework in red.

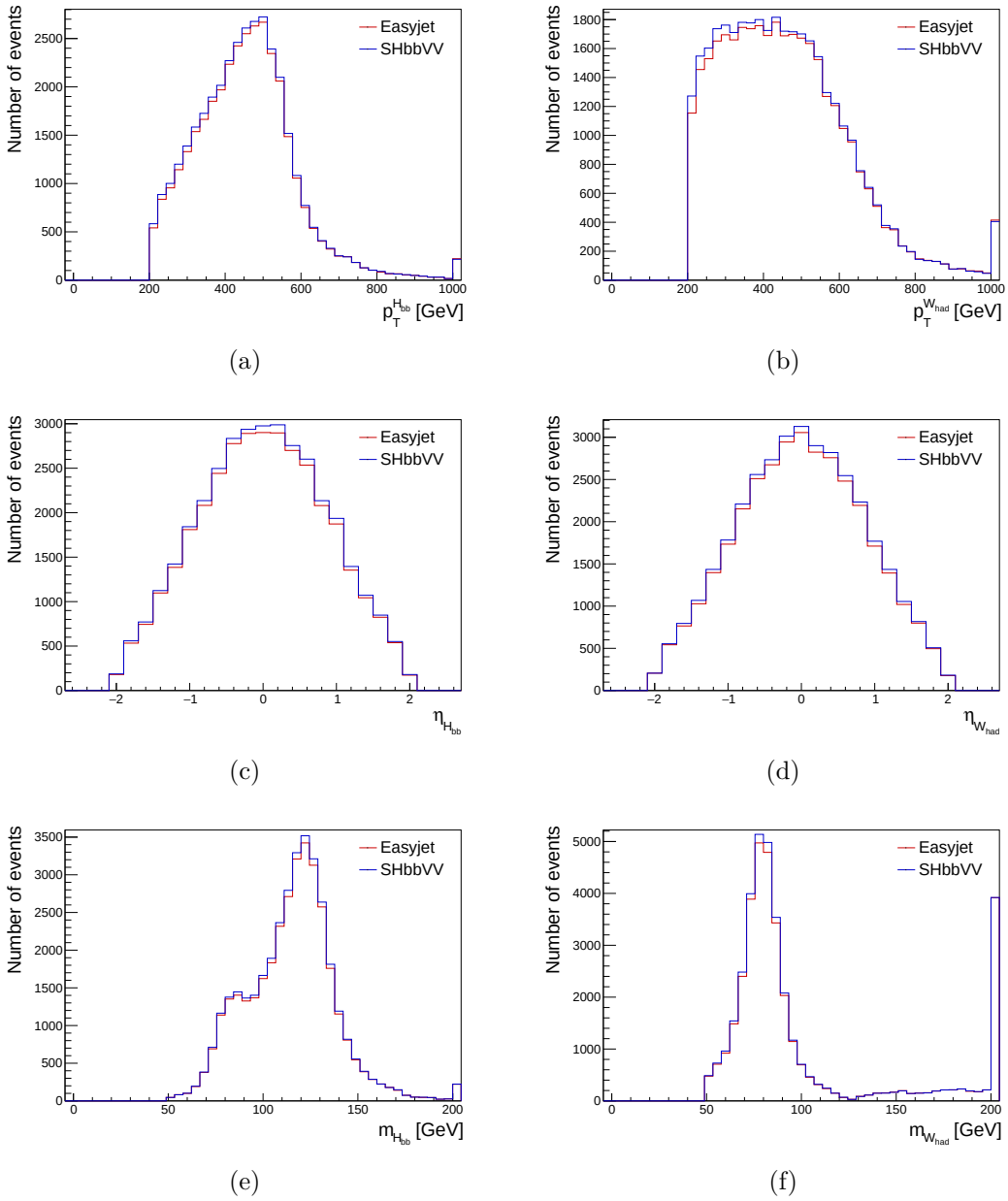

Figure B.8.: Distributions of the H_{bb} jet p_T (a), η (c) and mass (e) and W_{had} jet p_T (b), η (d) and mass (f) for the $m_X = 1500$GeV, $m_S = 750$ GeV mass point. The distributions are made after all selection criteria are applied on the events. Numbers from the SHbbVV framework are depicted in blue and from the easyjet framework in red.

Bibliography

[1] S. L. Glashow, *Partial Symmetries of Weak Interactions*, Nucl. Phys. **22**, 579 (1961)

[2] S. Weinberg, *A Model of Leptons*, Phys. Rev. Lett. **19**, 1264 (1967)

[3] A. Salam, *Weak and Electromagnetic Interactions*, Almqvist & Wiksell, Stockholm, nobel symposium 8 edition (1968)

[4] S. L. Glashow, et al., *Weak Interactions with Lepton-Hadron Symmetry*, Phys. Rev. D **2**, 1285 (1970)

[5] H. Georgi, S. L. Glashow, *Unified Weak and Electromagnetic Interactions without Neutral Currents*, Phys. Rev. Lett. **28**, 1494 (1972)

[6] H. D. Politzer, *Reliable Perturbative Results for Strong Interactions*, Phys. Rev. Lett. **30**, 1346 (1973)

[7] H. D. Politzer, *Asymptotic Freedom: An Approach to Strong Interactions*, Phys. Rep. **14**, 129 (1974)

[8] D. J. Gross, F. Wilczek, *Asymptotically Free Gauge Theories*, Phys. Rev. D **8**, 3633 (1973)

[9] ATLAS Collaboration, *Observation of a new particle in the search for the Standard Model Higgs boson with the ATLAS detector at the LHC*, Phys. Lett. B **716(1)**, 1 (2012)

[10] CMS Collaboration, *Observation of a new boson at a mass of 125 GeV with the CMS experiment at the LHC*, Phys. Lett. B **716(1)**, 30 (2012)

[11] M. B. Green, et al., *Superstring Theory: 25th Anniversary Edition*, Cambridge Monographs on Mathematical Physics, Cambridge University Press (2012)

[12] J. L. Feng, *Dark Matter Candidates from Particle Physics and Methods of Detection*, Annu. Rev. Astron. Astrophys. **48(1)**, 495 (2010)

[13] T. Robens, et al., *Two-real-scalar-singlet extension of the SM: LHC phenomenology and benchmark scenarios*, Eur. Phys. J. C **80(2)** (2020)

[14] S. Weinberg, *The Making of the Standard Model*, Eur. Phys. J. C **34**, 5 (2004)

[15] G. 't Hooft, *Renormalization of massless Yang-Mills fields*, Nucl. Phys. B **33(1)**, 173 (1971)

[16] G. 't Hooft, *Renormalizable Lagrangians For Massive Yang-Mills Fields*, Nucl. Phys. B **35**, 167 (1971)

[17] G. 't Hooft, M. Veltmann, *Regularization And Renormalization Of Gauge Fields*, Nucl. Phys. B **44**, 189 (1972)

[18] G. 't Hooft, M. Veltmann, *Combinatorics of gauge fields*, Nucl. Phys. B **50**, 318 (1972)

[19] P. W. Higgs, *Broken Symmetries, Massless Particles and Gauge Fields*, Phys. Lett. **12**, 132 (1964)

[20] F. Englert, R. Brout, *Broken Symmetry and the Mass of Gauge Vector Mesons*, Phys. Rev. Lett. **13**, 321 (1964)

[21] P. W. Higgs, *Broken Symmetries and the Masses of Gauge Bosons*, Phys. Rev. Lett. **13**, 508 (1964)

[22] G. S. Guralnik, et al., *Global Conservation Laws and Massless Particles*, Phys. Rev. Lett. **13**, 585 (1964)

[23] P. W. Higgs, *Spontaneous Symmetry Breakdown without Massless Bosons*, Phys. Rev. **145**, 1156 (1966)

[24] T. W. B. Kibble, *Symmetry Breaking in Non-Abelian Gauge Theories*, Phys. Rev. **155**, 1554 (1967)

[25] R. L. Workman, et al. (Particle Data Group), *Review of Particle Physics*, PTEP **2022**, 083C01 (2022)

[26] H. Fritzsch, et al., *Advantages of the color octet gluon picture*, Phys. Lett. B **47(4)**, 365 (1973)

[27] M. Gell-Mann, *A Schematic Model of Baryons and Mesons*, Phys. Lett. **8**, 214 (1964)

[28] E. Eichten, et al., *Charmonium: The model*, Phys. Rev. D **17**, 3090 (1978)

[29] D. J. Gross, F. Wilczek, *Ultraviolet Behavior of Non-Abelian Gauge Theories*, Phys. Rev. Lett. **30**, 1343 (1973)

[30] K. G. Wilson, *Confinement of quarks*, Phys. Rev. D **10**, 2445 (1974)

[31] S. Tomonaga, *On a Relativistically Invariant Formulation of the Quantum Theory of Wave Fields**, Progr. Theor. Phys. **1(2)**, 27 (1946)

[32] J. Schwinger, *On Quantum-Electrodynamics and the Magnetic Moment of the Electron*, Phys. Rev. **73**, 416 (1948)

[33] J. Schwinger, *Quantum Electrodynamics. I. A Covariant Formulation*, Phys. Rev. **74**, 1439 (1948)

[34] R. P. Feynman, *Space-Time Approach to Quantum Electrodynamics*, Phys. Rev. **76**, 769 (1949)

[35] R. P. Feynman, *The Theory of Positrons*, Phys. Rev. **76**, 749 (1949)

[36] R. P. Feynman, *Mathematical Formulation of the Quantum Theory of Electromagnetic Interaction*, Phys. Rev. **80**, 440 (1950)

[37] F. J. Dyson, *The Radiation Theories of Tomonaga, Schwinger, and Feynman*, Phys. Rev. **75**, 486 (1949)

[38] F. J. Dyson, *The S Matrix in Quantum Electrodynamics*, Phys. Rev. **75**, 1736 (1949)

[39] N. Cabbibo, *Unitary Symmetry and Leptonic Decays*, Phys. Rev. Lett. **10**, 531 (1963)

[40] M. Kobayashi, T. Maskawa, *CP Violation in the Renormalizable Theory of Weak Interaction*, Prog. Theor. Phys. **49**, 652 (1973)

[41] S. Weinberg, *General Theory of Broken Local Symmetries*, Phys. Rev. D **7**, 1068 (1973)

[42] B. D. Micco, et al., *Higgs boson potential at colliders: Status and perspectives*, Rev. Phys. **5**, 100045 (2020)

[43] ATLAS Collaboration, *Search for non-resonant Higgs boson pair production in the $bb\ell\nu\ell\nu$ final state with the ATLAS detector in pp collisions at $\sqrt{s} = 13$ TeV*, Phys. Lett. B **801**, 135145 (2020)

[44] G. Branco, et al., *Theory and phenomenology of two-Higgs-doublet models*, Phys. Rep. **516(1)**, 1 (2012)

[45] A. Azatov, et al., *Effective field theory analysis of double Higgs boson production via gluon fusion*, Phys. Rev. D **92**, 035001 (2015)

[46] P. Huang, et al., *Corrections to di-Higgs boson production with light stops and modified Higgs couplings*, Phys. Rev. D **97**, 075001 (2018)

[47] V. Barger, et al., *CERN LHC phenomenology of an extended standard model with a real scalar singlet*, Phys. Rev. D **77**, 035005 (2008)

[48] L. R. Evans, P. Bryant, *LHC Machine*, JINST **3**, S08001 (2008)

[49] E. Mobs, *The CERN accelerator complex in 2019. Complexe des accélérateurs du CERN en 2019* (2019), general Photo

[50] ATLAS collaboration, *The ATLAS Experiment at the CERN Large Hadron Collider*, JINST **3**, S08003 (2008)

[51] K. Abeling, *Search for resonant Higgs boson pair production in the $b\bar{b}WW^*$ decay channel in the boosted 1-lepton final state using the full Run 2 ATLAS dataset*, Ph.D. thesis, Georg-August-Universität Göttingen (2022)

[52] K. Abeling, et al., *Search for resonant boosted HH and SH production in the bbVV decay channel with 0 or 1 lepton in the final state using the full Run 2 ATLAS data*, Technical report, CERN, Geneva (2022)

[53] ATLAS Collaboration, *Electron and photon performance measurements with the ATLAS detector using the 2015–2017 LHC proton-proton collision data*, JINST **14(12)**, P12006 (2019)

[54] *ATLAS Isolation and Fake Forum*, [Last accessed: 13-February-2024], URL `https://atlas-iff.docs.cern.ch/rel22recommendedisowps/index.html`

[55] ATLAS Collaboration, *Muon reconstruction and identification efficiency in ATLAS using the full Run 2 pp collision data set at $\sqrt{s} = 13$ TeV*, Eur. Phys. J., C **81**, 578 (2021)

[56] M. Cacciari, et al., *The anti-ktjet clustering algorithm*, J. High Energy Phys. **2008(04)**, 063–063 (2008)

[57] ATLAS Collaboration, *Performance of b-jet identification in the ATLAS experiment*, JINST **11(04)**, P04008–P04008 (2016)

[58] J. Barr, *Working Points, New Top Labels and Resurrecting Subjets* (2023), URL `https://indico.cern.ch/event/1293204/contributions/5435088/attachments/2659450/4606521/2023-06-05-TaskForce-Update.pdf`

Acknowledgement

First of all, I would like to thank Prof. Dr. Stan Lai, who made it possible to write my Bachelor's thesis in his research group. The weekly research chat really helped the progress of this thesis and gave great input. Additionally, I would like to thank Prof. Dr. Ariane Frey for being my second referee.
A big thank you goes to Dr. Kira Abeling, who answered all my questions at all times (really ALL times), even though she had more than enough to do herself. She also saved this bachelor thesis by lending me her old laptop a few weeks before submission, after mine suffered an involuntary tea shower. I would also like to thank L*na, who were always willing to answer my questions.
Special thanks go to my friends from the "Glaskasten", who put up with me even during the stressful phases and always brought me food from the "Z-" or "Turm Mensa" when I didn't have time to go myself. I'd also like to thank my lovely flatmates, who sometimes overlooked that I didn't keep to the cleaning schedule quite so conscientiously.
Last but not least, I would like to thank my parents and my sister, who always supported me, even though I often emptied the fridge when I was at home.

Erklärung nach §13(9) der Prüfungsordnung für den Bachelor-Studiengang Physik und den Master-Studiengang Physik an der Universität Göttingen:
Hiermit erkläre ich, dass ich diese Abschlussarbeit selbständig verfasst habe, keine anderen als die angegebenen Quellen und Hilfsmittel benutzt habe und alle Stellen, die wörtlich oder sinngemäß aus veröffentlichten Schriften entnommen wurden, als solche kenntlich gemacht habe.
Darüberhinaus erkläre ich, dass diese Abschlussarbeit nicht, auch nicht auszugsweise, im Rahmen einer nichtbestandenen Prüfung an dieser oder einer anderen Hochschule eingereicht wurde.

Göttingen, den 28. Mai 2024

(Monja Begau)